Atmos. Meas. Tech., 9, 4759–4781, 2016
www.atmos-meas-tech.net/9/4759/2016/
doi:10.5194/amt-9-4759-2016

Atmospheric Measurement Techniques
Open Access
EGU

A semiempirical error estimation technique for PWV derived from atmospheric radiosonde data

Julio A. Castro-Almazán[1,2], **Gabriel Pérez-Jordán**[1], **and Casiana Muñoz-Tuñón**[1,2]

[1]Instituto de Astrofísica de Canarias, 38200, La Laguna, Spain
[2]Dept. Astrofísica, Universidad de La Laguna, 38200, La Laguna, Spain

Correspondence to: Julio A. Castro-Almazán (jcastro@iac.es)

Received: 13 November 2015 – Published in Atmos. Meas. Tech. Discuss.: 15 February 2016
Revised: 25 July 2016 – Accepted: 29 July 2016 – Published: 26 September 2016

Abstract. A semiempirical method for estimating the error and optimum number of sampled levels in precipitable water vapour (PWV) determinations from atmospheric radiosoundings is proposed. Two terms have been considered: the uncertainties in the measurements and the sampling error. Also, the uncertainty has been separated in the variance and covariance components. The sampling and covariance components have been modelled from an empirical dataset of 205 high-vertical-resolution radiosounding profiles, equipped with Vaisala RS80 and RS92 sondes at four different locations: Güímar (GUI) in Tenerife, at sea level, and the astronomical observatory at Roque de los Muchachos (ORM, 2300 m a.s.l.) on La Palma (both on the Canary Islands, Spain), Lindenberg (LIN) in continental Germany, and Ny-Ålesund (NYA) in the Svalbard Islands, within the Arctic Circle. The balloons at the ORM were launched during intensive and unique site-testing runs carried out in 1990 and 1995, while the data for the other sites were obtained from radiosounding stations operating for a period of 1 year (2013–2014). The PWV values ranged between $\sim$ 0.9 and $\sim$ 41 mm. The method sub-samples the profile for error minimization. The result is the minimum error and the optimum number of levels.

The results obtained in the four sites studied showed that the ORM is the driest of the four locations and the one with the fastest vertical decay of PWV. The exponential autocorrelation pressure lags ranged from 175 hPa (ORM) to 500 hPa (LIN). The results show a coherent behaviour with no biases as a function of the profile. The final error is roughly proportional to PWV whereas the optimum number of levels (N_0) is the reverse. The value of N_0 is less than 400 for 77 % of the profiles and the absolute errors are always < 0.6 mm. The median relative error is 2.0 ± 0.7 % and the 90th percentile $P_{90} = 4.6$ %. Therefore, whereas a radiosounding samples at least N_0 uniform vertical levels, depending on the water vapour content and distribution of the atmosphere, the error in the PWV estimate is likely to stay below ≈ 3 %, even for dry conditions.

1 Introduction

Although the water vapour (WV) accounts for only 0–4 % of all atmospheric molecules, it is a powerful greenhouse gas, with strong lines of absorption and emission in the infrared (IR). Atmospheric WV also participates in processes affecting the global climate (Elliott and Gaffen, 1995; Ahrens, 2003) and is the principal molecule responsible for atmospheric extinction in IR astronomical observations, especially at wavelengths longer than $\sim$15 microns (far IR), in several bands in the middle and near IR, as well as in the submillimetre and microwave range (Selby and Mampaso, 1991; Hammersley, 1998; García-Lorenzo et al., 2010; Otárola et al., 2010).

The total amount of WV above a particular location is highly variable and can be expressed as the precipitable water vapour (PWV), which is defined as the total water column height when integrated from the surface to the top of the atmosphere with unit cross section[1]. PWV is commonly expressed in millimetres, in terms of the height to which that water would stand if completely condensed and collected in a vessel with a cross section of 1 m^2.

[1]http://glossary.ametsoc.org/wiki/Precipitable_water

PWV can be measured by radiosounding balloons, radiometers from both ground (Fowle, 1912; Guiraud et al., 1979; Carilli and Holdaway, 1999; Smith et al., 2001) and satellites (Grody et al., 1980; Menzel et al., 1998; Gao and Kaufman, 2003; Deeter, 2007; Wong et al., 2015), sun photometers (Bird and Hulstrom, 1982; Volz, 1983; Plana-Fattori et al., 1998; Firsov et al., 2013), lunar photometers (Barreto et al., 2013), GPS receivers (Bevis et al., 1992, 1994), Fourier transform infrared spectrometers (Kurylo, 1991; Schneider et al., 2006) and others (Schneider et al., 2010). Of these techniques, atmospheric radiosoundings are a direct in situ measurement and one of the most accurate methods of retrieving the PWV. Radiosoundings are also one of the current standards for atmospheric research and are widely used as a valid reference for comparison and calibration. Therefore, a proper error estimation of PWV obtained from radiosoundings is extremely important. Previous works have dealt with the issue of the accuracy of radiosonde measurements of PWV, including experimental errors and differences in sensor output because of variations in wetness in the column or sensor types (see, for example, Miloshevich et al., 2006, or Romero-Campos et al., 2011). Nevertheless, as radiosondes provide a discrete profiling of the atmospheric column, other important factors impacting the final error in PWV measurements, such as the propagation of uncertainties and vertical sampling, have to be taken into account (Liu et al., 2000). These latter error sources have not yet been explored in depth and are the subject of this paper.

1.1 Rationale and objectives

Accurate error estimation of PWV from radiosoundings is essential for regression analyses in comparison or calibration studies. In this sense, special care is needed when radiosoundings from different sources and with differing characteristics are being discussed, or when working in a particularly dry atmosphere. This was the case in Pérez-Jordán et al. (2015), where we used a set of 23 high-vertical-resolution balloons to validate the Weather Research and Forecasting (WRF) mesoscale numerical model for a dry astronomical location (Roque de los Muchachos Observatory, Canary Islands, Spain; ORM hereafter). The possibility of making use of these radiosounding datasets provided a unique opportunity, as no other atmospheric balloons had been launched at the observatory.

A second sample of 42 radiosoundings were also included in Pérez-Jordán et al. (2015) for verification and control. The point selected was the radiosounding operational station located close to sea level in Güímar (GUI, hereafter), in the neighbouring island of Tenerife. The data were downloaded from the repository maintained by the Department of Atmospheric Science of the University of Wyoming[2] (WYO hereafter). Both the ORM and GUI-WYO datasets showed strong differences in sampling (~ 100 levels at GUI-WYO versus more than 2500 at ORM) as a consequence of the reencoding applied at WYO.

In the present work, we are using the same dataset of high-vertical-resolution radiosounding flights at ORM and GUI to model the error in PWV calculations from balloons and we propose a method to retrieve it. The dataset at GUI has been extended to 62 profiles. In this study we obtained the data from the Spanish State Meteorological Agency (AEMet) to include all the available operational data points (> 2500). To extend the validity of the work, we have included two equivalent datasets from two locations: Lindenberg (LIN), in Germany, and Ny-Ålesund (NYA) in the Svalbard Islands, Norway. See Sect. 1.2 for a detailed description of all the locations and databases.

The method considers two components in the error estimation for PWV obtained from radiosoundings: the propagated uncertainties in the measures and the sampling error. We estimated the uncertainty contribution by means of analytical error propagation through all the levels sampled by the balloon. The propagation includes the covariance with the incoming pressure levels, which was empirically modelled from the autocorrelation function for each location. The sampling component has also been modelled from the high-resolution datasets.

Since the method is based on models empirically fitted to local data, we obtained parameters that are valid for the four sites considered. Nevertheless, the proposed method is general and may be extended to any other location by introducing its local data into the models. The results cover a wide variety of conditions originating from the different path lengths (departures from 5 to ~ 2200 m a.s.l.), PWV content ($\sim$ 1–40 mm) and troposphere conditions (latitudes 28, 52 and 79° N). The result also includes an estimate of the optimum number of sampled levels needed to fit into the minimum error.

To validate the method for different samplings, the standard (SD) and significant (SIG) levels have been extracted from a subset of 42 radiosoundings from GUI. The SD levels are the basic pressure levels for which the radiosounding data are submitted. They correspond to 1000, 925, 850, 700, 500, 400, 300, 250, 200, 150, 100, 70, 50, 30, 20 and 10 hPa, although the last ones are not always reported, depending on the top height reached by the balloon (≈ 15 levels). The SIG codification provides ≈ 30 additional measurements to ensure that the linear interpolation between adjacent levels is not missing significant changes in the profiles. The coding rules allow linear interpolations between SIG points to differ from the original measurements by up to ± 1 K for temperature and up to ± 15 % for relative humidity in the troposphere (up to ~ 300 hPa) and up to ± 2 K for temperature in the stratosphere. Finally, the same profiles, downloaded from WYO, which are encoded to ~ 100 significant levels, have also been included in the validation. The method was applied to the most pessimistic case, considering only the SD

[2] http://weather.uwyo.edu/upperair/sounding.html

levels, to the SIG levels alone, the SD + SIG and the WYO re-encoded sub-samplings.

1.2 Locations and datasets

The balloons were launched at four separated locations (see Fig. 1): Roque de los Muchachos Observatory (28.76° N, 17.89° W; 2200 m a.s.l.) on La Palma and Güímar (28.32° N, 16.38° W; 105 m a.s.l.) in Tenerife (both in the Canary Islands, Spain), Lindenberg (52.21° N, 14.12° E; 98 m a.s.l.) in northern Germany, and Ny-Ålesund (78.92° N, 11.92° E; 5 m a.s.l.) in the Svalbard Islands, Norway.

The ORM is one of the most competitive astronomical observatories on Earth (see Vernin et al., 2011 for a review); it hosts, among others, the largest optical-IR telescope in the world, the 10.4 m Gran Telescopio Canarias (GTC). The altitude at the ORM ranges from ∼ 2200 to ∼ 2400 m a.s.l., balloons being launched from the lowest level.

The ORM data come from a unique dataset obtained during intensive site-testing assessments performed in April 1990, July 1990 and November 1995 in a joint run carried out by the Instituto de Astrofísica de Canarias and the University of Nice with support of the Centre National de Recherches Météorologiques (Météo-France). The details of these campaigns are described in Vernin and Muñoz-Tuñón (1992, 1994). A total of 23 balloons were launched from the observatory, 22 of them being selected to model the error, after rejecting the one that did not cover the whole troposphere. The profiles provide a dataset of very high vertical resolution with 2500 to 7000 data points per balloon flight.

Because of their latitude and eastern location in the North Atlantic Ocean, the Canary Islands exhibit a vertical troposphere structure with a trade wind thermal inversion layer (IL), driven by subsiding cool air from the descending branch of the Hadley cell. The altitude of the IL ranges on average from 800 m in summer to 1600 m in winter, well below the altitude of the ORM (Dorta, 1996; Carrillo et al., 2016). The IL separates the moist marine boundary layer from the dry free atmosphere, inducing very high atmospheric stability above it. Therefore, the PWV values at both locations in the Canary Islands (GUI and ORM) are strongly uncorrelated with wide differences in their atmospheric conditions. The average mesoscale conditions in the Canary Islands show a relative humidity profile under the IL that drops drastically with increasing altitude. Temperatures below −40 °C are typically reached above 8 km in the troposphere.

GUI is the closest radiosonde operational station to ORM, located ≈ 155 km away and closest to sea level. It is an AEMet station, part of the World Meteorological Organization (WMO) network, code 60018[3]. The sample from GUI covers 1 year of data with a total of 62 operational radiosoundings, mainly from May 2013 to April 2014. The balloons at GUI are routinely launched twice daily (at 00:00 and 12:00 UTC) by the AEMet. The significant level assignment for GUI, used for validation in Sect. 5.4, was carried out by the AEMet following WMO standards (see Sect. 1.1).

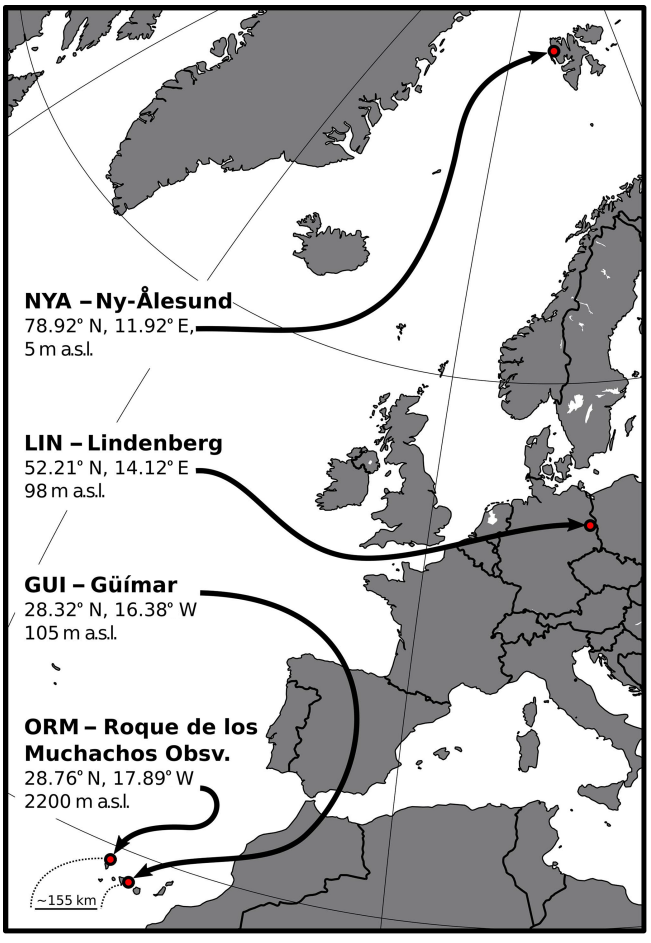

Figure 1. Location and height above the sea level of the four radiosounding launching points in the Canary Islands, Spain (ORM and GUI), separated by ≈ 155 km, Lindenberg in Germany, and Ny-Ålesund, in the Svalbard Islands, Norway (source: Wikimedia Commons).

The LIN and NYA observatories are certified stations of the GCOS (Global Climate Observing System) Reference Upper-Air Network (GRUAN)[4] and are also part of the WMO network. LIN is a climate reference site of the Deutscher Wetterdienst (DWD) and hosts the GRUAN Lead Centre. The balloons are routinely launched every 6 h. LIN is located in an all-year-wet, maritime temperate climate[5]. NYA is an atmospheric research observatory operated by the Alfred-Wegener-Institut für Polarforschung (AW) and the Helmholtz Centre Potsdam German Research Centre for Geosciences (GFZ). The balloons are launched at an approx-

[3] http://weather.gladstonefamily.net/site/60018

[4] http://www.dwd.de/EN/research/international_programme/gruan/home.html

[5] https://www.wmo.int/pages/prog/www/IMOP/TB_LC/LeadCenter_Germany.html

imate rate of one per day. NYA is in a climatic-strategic location at the gateway to the Arctic Ocean. The data compiled from LIN and NYA are statistically equivalent to the dataset from GUI, with 58 and 63 soundings, ranging from May 2013 to April 2014.

1.3 Instrumental set-up

The radiosondes used were a Vaisala RS80 at ORM (1990 and 1995) and a Vaisala RS92 for the other operational soundings (2013–2014). In both cases, the sondes were calibrated during the ground check immediately before the balloon release. The standard Vaisala procedure for sonde preparation and systematic error source minimization were followed, together with various corrections for daytime solar heating. For an extensive characterization of both radiosonde set-ups see Miloshevich et al. (2001, 2009). In the particular case of GUI, more details of the corrections applied are given in Romero-Campos et al. (2011). The quality controls for GRUAN (LIN and NYA) are detailed in Immler et al. (2010) and Dirksen et al. (2014).

The uncertainties assumed in this work for both radiosondes are $\pm 0.5\,^{\circ}\mathrm{C}$, $\pm 5\,\%$ and $\pm 1\,\mathrm{hPa}$ for temperature, relative humidity and atmospheric pressure. These values are in agreement with the estimates for the RS92 obtained within the extensive network of GRUAN by Dirksen et al. (2014). The equations accept future improvements on sensor uncertainties, such as the inclusion of vertically resolved profiles of uncertainties (Dirksen et al., 2014) that the new binary encodings for radiosonde data, such as BUFR (Binary Universal Form for the Representation of meteorological data), are introducing (Dragosavac, 2007).

Both RS80 and RS92 suffer from time lag in the relative humidity sensor response that increases as temperature drops. The delay is caused by the slow response of the sensor (a film capacitor that acts as a dielectric) at low temperatures. As noted by Miloshevich et al. (2006), this time lag error is not a bias error but rather a *smoothing* of the profile by an amount that depends on the temperature and local humidity gradient. Such a time lag was studied and characterized by the empirical approximating expression of Miloshevich et al. (2001). The response time increases significantly in the upper troposphere for temp $< -68\,^{\circ}\mathrm{C}$ (Vömel et al., 2007), which is reached typically above 10 000 m, where the water vapour mixing ratio drastically drops, reducing the contribution to the total integrated PWV. Besides we can assume a uniform distribution in water vapour in the upper troposphere for the time delay. Under these conditions, the time lag has the effect of smoothing the signal and reducing the dispersion, without significantly moving the average and therefore not impacting on the total PWV in the column.

2 PWV from radiosondes

The PWV is obtained from the temperature T (°C), atmospheric pressure p (hPa) and relative humidity RH (%) measured by the radiosondes (Curry and Webster, 1999). Following the definition given in Sect. 1, the PWV can be expressed by

$$\mathrm{PWV} = \frac{10^3}{\rho} \int_{z=0}^{z=\infty} \rho_{\mathrm{w}} dz \qquad (\mathrm{mm}), \tag{1}$$

where z is the height in m, and ρ and ρ_{w} are the liquid water and WV densities, both in $\mathrm{kg\,m^{-3}}$. The definition of the WV mixing ratio r is

$$r = \frac{m_{\mathrm{w}}}{m_{\mathrm{d}}} = \frac{\rho_w}{\rho_{\mathrm{d}}}, \tag{2}$$

where m_{w} and ρ_{w} are the WV mass and density, and m_{d} and ρ_{d} are the corresponding values for dry air. We can assume hydrostatic balance ($\mathrm{d}p = -\rho_{\mathrm{d}} \cdot g \cdot \mathrm{d}z$) and write Eq. (1) in the form

$$\mathrm{PWV} = \frac{10^5}{\rho g} \int_{p_{\mathrm{t}}}^{p_{\mathrm{s}}} r \mathrm{d}p \qquad (\mathrm{mm}), \tag{3}$$

where g is the Earth's gravity ($\mathrm{m\,s^{-2}}$) and p_{s} and p_{t} are the pressure at the surface and at the top of the sampled atmospheric column in hPa. We can now apply the ideal gas law and Dalton's law of partial pressures to Eq. (2) to get

$$r = 0.622 \left(\frac{e}{p - e} \right). \tag{4}$$

The coefficient 0.622 is the molecular mass ratio of WV in dry air and e is the partial vapour pressure that can be obtained from the definition of relative humidity as

$$e = e_{\mathrm{sat}} \cdot \frac{\mathrm{RH}}{100} \qquad (\mathrm{hPa}). \tag{5}$$

Finally, the saturation vapour pressure e_{sat} can be expressed as an empirical polynomial fit, following Curry and Webster (1999):

$$\begin{aligned} e_{\mathrm{sat}} = & a_0 + T\,(a_1 + T \\ & \ldots + T\,(a_4 + T\,(a_5 + T a_6))\ (\mathrm{hPa}). \end{aligned} \tag{6}$$

The coefficients a_i have been taken from Flatau et al. (1992) (see Table 1).

Table 1. Saturation vapour pressure coefficients and associated uncertainties (Flatau et al., 1992).

a_j	Coefficient	Uncertainty
a_0	6.11176750	$4.44010270 \times 10^{-1}$
a_1	$4.43986062 \times 10^{-1}$	$2.86175435 \times 10^{-2}$
a_2	$1.43053301 \times 10^{-2}$	$7.95246610 \times 10^{-4}$
a_3	$2.65027242 \times 10^{-4}$	$1.20785253 \times 10^{-5}$
a_4	$3.02246994 \times 10^{-6}$	$1.01581498 \times 10^{-7}$
a_5	$2.03886313 \times 10^{-8}$	$3.84142063 \times 10^{-10}$
a_6	$6.38780966 \times 10^{-11}$	$6.69517837 \times 10^{-14}$

3 Error budget for PWV from radiosonde data

The integral in Eq. (3) is computed as a discrete summation (following a trapezoidal method) over all the levels sampled by the radiosonde. We can write the final error associated with the PWV determination, ϵ_{f}, as

$$\epsilon_{\mathrm{f}}^2 = \sigma^2 + \epsilon_{\mathrm{s}}^2. \tag{7}$$

The last term (ϵ_{s}) is the sampling error and σ is the uncertainty in the measurement, which can be written as

$$\sigma^2 = \mathrm{var_f} + 2 \cdot \mathrm{cov_f} = \sum_{i=0}^{N-1} \sigma_i^2 + 2 \sum_{i,j;\, j>i} \sigma_i \sigma_j \rho_{ij} \quad (\mathrm{mm}^2), \tag{8}$$

where $\mathrm{var_f}$ is the final variance, expressed as the sum of the variances at each level, σ_i^2, and $\mathrm{cov_f}$ is the covariance as a function of the autocorrelation between levels ρ_{ij}.

3.1 Uncertainty propagation: variance component

Let $\sigma_{p,i}$, $\sigma_{T,i}$ and $\sigma_{\mathrm{RH},i}$ be the instrumental uncertainties associated with the direct measure of the atmospheric pressure p, temperature T and relative humidity RH at a certain level i. The variance of PWV can be obtained by error propagation over all the sampled levels N in Eq. (3). Nevertheless, each value, excluding the extremes, is shared by adjacent bins; therefore, the derivation of the variance must avoid the double summation (see details in Appendix A). Assuming p and r to be independent, we can write the variance of the trapezoidal expansion of Eq. (3) as in Eq. (A3):

$$\mathrm{var_f} = \sigma_r^2 + \sigma_p^2 \qquad (\mathrm{mm}^2). \tag{9}$$

The variances of the water vapour mixing ratio, r (σ_r^2), and pressure, p (σ_p^2), may be obtained from the Eqs. (A7) and (A9):

$$\sigma_p^2 = \left(\frac{10^5}{2\rho g}\right)^2 \left[\sigma_{p,0}^2 (r_1 + r_0)^2 + \sigma_{p,N}^2 (r_N + r_{N-1})^2 + \sum_{i=0}^{N-1} \sigma_{p,i}^2 (r_{i+1} - r_{i-1})^2\right] \quad (\mathrm{mm}^2), \tag{10}$$

$$\sigma_r^2 = \left(\frac{10^5}{2\rho g}\right)^2 \left[\sigma_{r,0}^2 (p_1 - p_0)^2 + \sigma_{r,N}^2 (p_N - p_{N-1})^2 + \sum_{i=0}^{N-1} \sigma_{r,i}^2 (p_{i+1} - p_{i-1})^2\right] \quad (\mathrm{mm}^2), \tag{11}$$

where p_i and r_i are the pressure and mixing ratio at level i. By a recursive use of the error propagation rules in Eqs. (4), (5) and (6), the following expressions are obtained for the uncertainties $\sigma_{r,i}$, $\sigma_{e,i}$ and $\sigma_{e_{\mathrm{sat}},i}$:

$$\sigma_{r,i}^2 \approx \left(0.622 \cdot \frac{\sigma_{e,i}}{p_i}\right)^2, \tag{12}$$

$$\sigma_{e,i}^2 = 10^{-4} \left[\left(\mathrm{RH}_i \cdot \sigma_{e_{\mathrm{sat}},i}\right)^2 + \left(e_{\mathrm{sat},i} \cdot \sigma_{\mathrm{RH},i}\right)^2\right] \quad (\mathrm{hPa}^2), \tag{13}$$

$$\sigma_{e_{\mathrm{sat}},i}^2 = \sum_{j=0}^{6} \left[\left(T_i^j \cdot \sigma_{a,j}\right)^2 + \left(a_j \cdot j \cdot T_i^{j-1} \cdot \sigma_{T,i}\right)^2\right] \quad (\mathrm{hPa}^2), \tag{14}$$

where a_j and $\sigma_{a,j}$ are the seven ($j = 0, 6$) saturation vapour pressure coefficients and the associated uncertainties for each sampled level i (see Table 1). The contribution of the covariances between variables in the propagation of errors was specifically calculated, leading to negligible values less than 10^{-3} mm, and is therefore not included in Eqs. (9)–(14).

3.2 Uncertainty propagation: covariance component

We may consider the vertical profiles as *time series* generated by the balloon flights (*space series*). Each observation of the sensors on board the balloon may be viewed as the only possible realization of the physical process governing the atmosphere at this point and time. Therefore, each measurement at a particular height during the flight will be a random value within the accuracy of the sensor that can be assumed as a semi-Markov process, where the influence on the error of the next levels may be modelled through the covariance (see Eq. 8) as a simplified pure exponential autocorrelation function:

$$\mathrm{cov_f} = \sum_{i,j;\, j>i} \sigma_i \sigma_j \rho_{ij} = \sigma_i \sigma_j e^{-(p_i - p_j)/\tau_\rho} \qquad (\mathrm{mm}^2), \tag{15}$$

where the exponential autocorrelation pressure lag (τ_ρ) was empirically determined for each location after obtaining the

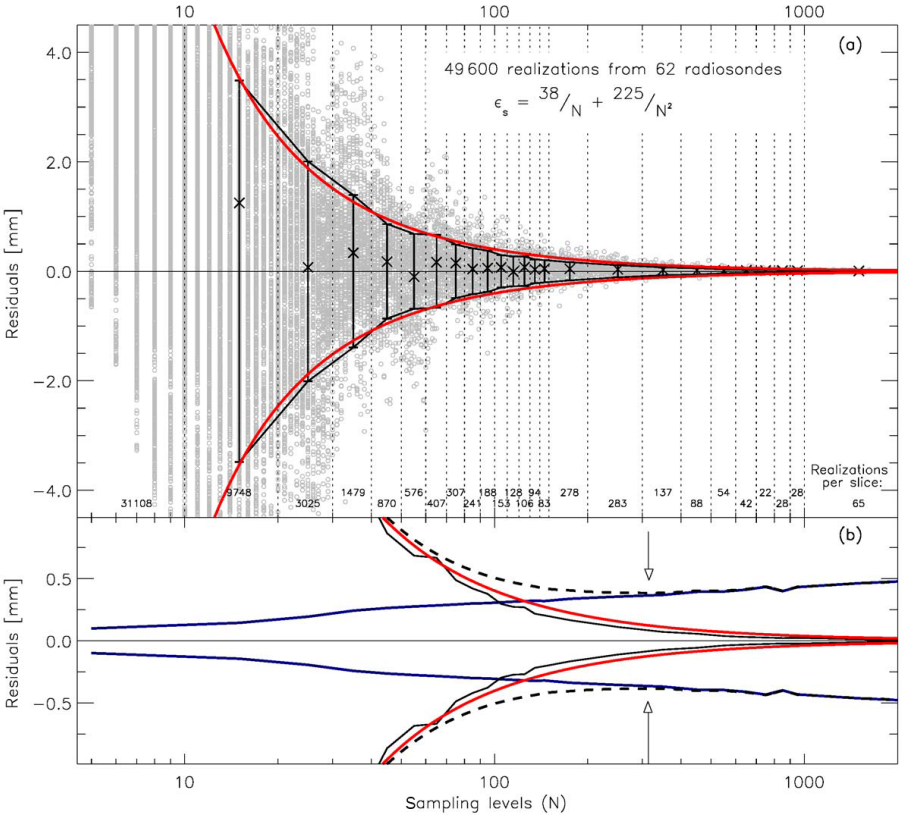

[t]

Figure 2. (a) Example of sampling error modelling for PWV radiosondes, as a function of the number of levels (see Fig. 4 to see the model fitting for all the sites). The profiles are gradually sub-sampled to obtain a large number of realizations of PWV (grey circles). The error is then fitted (red solid lines; see Eq. 18) to the RMSE of the residuals (see Eq. 16) in sliced (dotted lines) sampling levels. The error bars show the RMSE per slice and the "x" symbols are the bias. **(b)** Sub-sampling error optimization. The solid black line is the experimental sample error as a function of the number of levels and the red line is the model (same as in panel **a** but with trimmed y axis). The blue line is the median of the propagated uncertainties (Eq. 8) for all the profiles and the dashed line is the final error (Eq. 7). The arrows show the optimized number of samples for the minimum error.

autocorrelations ρ_{ij} between a sub-sample of r_i and r_j, separated by the lag $p_i - p_j$, from all the available radiosoundings. The lag was recursively increased while $\rho_{ij} \geq 0.2$. For a fixed time lag, the departure levels i were sequentially shifted up to a top limit such as level + lag, approximately reaching the tropospheric height where the content of water vapour drops. Finally the average autocorrelation decay curve was fitted to an exponential function $\exp[-(p_i - p_j)/\tau_\rho]$. In Sect. 5.1 we show the results for each location.

3.3 Sampling error

The number of levels included for PWV determinations from atmospheric radiosondes may range from tens (when only standard levels are available) to thousands (full profile). All the high-resolution profiles compiled in this study range from $\sim$2500 to $\sim$7000 data points, dense enough to neglect the sampling error. This circumstance allowed us to empirically obtain an expression for ϵ_s as a function of the number of sampled levels N, following a recursive sub-sampling process.

Each profile was uniformly sub-sampled at equal intervals by taking one point in two, one in three, etc., to obtain 800 different realizations of PWV for the same profile (any other uniform sub-sampling is valid). The dispersion of the residuals increases logarithmically as the number of levels N decreases (see Fig. 2a for an example at GUI), with the residuals defined as

$$\mathrm{res}_N = I - \widetilde{I}_N, \tag{16}$$

where I and $\widetilde{I}_N$ are the integral in Eq. (3) calculated with all the levels in the profile ($N_{\max}$) and with the different realizations of N levels after the sub-sampling process. The residuals were grouped in slices for intervals of N to fit a model. The size of the slices was selected following a quasi-logarithmic scale to overcome the differences in variance (heteroscedasticity) while conserving the statistical significance (see Fig. 2a for details of the slices and the number of residuals included for each). The sampling error was then

obtained as the root-mean-square error (RMSE) of the residuals for each slice. The RMSE was calculated as the square root of the sum of the variance and the squared bias for every interval.

The dependence on N of res_N comes from the integrals $\widetilde{I}_N$ in Eq. (16) in the form

$$\widetilde{I}_N = \widetilde{\mathrm{PWV}}(N^{-1}) + E(N^{-2}), \tag{17}$$

where the first term, $\widetilde{\mathrm{PWV}}$, is the composite trapezoidal sum of Eq. (3) sub-sampled to N levels and the second one is the associated error. Therefore, taking N as the middle point of each slice interval in Fig. 2a, we modelled the residual (Eq. 16) behaviour by fitting a function $A/N + B/N^2 + C$ to the RMSEs, with the coefficient $C = 0$, as $\lim_{(N\to\infty)}\mathrm{res}_N = 0$. Finally, we applied a gradient-expansion algorithm to compute a nonlinear least squares fit to obtain the coefficients s_0 and s_1 (red line in Fig. 2).

$$\epsilon_\mathrm{s} = \frac{s_0}{N} + \frac{s_1}{N^2}; \quad (N \gtrsim 10) \tag{18}$$

In Sect. 5.2 we show the results for each location. Equation (18) assumes that the radiosounding is uniformly sampling the whole atmosphere where the PWV concentrates (mainly the lower and mid-troposphere). The limit depends on each particular site but it may be established in ≈ 20 km. All the radiosoundings in the present study fulfil this condition except for ORM-VOL18, which reached 17 797 m and was included after a visual inspection (see Appendix B for a compilation of all the data). The bias induced by the shortage in height profiling is beyond the scope of this paper, as it would need a detailed model (with larger samples) of the probability of missing high-altitude wet layers, depending on the local troposphere and season. These models may also allow for alternative nonuniform sub-samplings, concentrating the measured levels where a priori a less uniform PWV distribution is to be expected (i.e. that would most impact on the sampling error).

4 Optimized error

The two components in Eq. (7) behave contrary to the number of sampled levels. Because of the exponential decay in the autocorrelation, the closer the levels, the larger the covariance contribution to the final error and the less the information obtained to the final integrated PWV. Therefore, σ increases with the number of levels in the profile. In contrast, the sampling error is in the opposite direction and ϵ_s increases as the number of sampled levels decreases. This behaviour is described in Fig. 2b, which shows the sampling error ϵ_s fitted in Eq. (18) and the median σ calculated as a function of the sampling levels N for each slice of sub-sampled data.

Therefore, it is always possible to sub-sample the profile uniformly, obtaining $\epsilon_\mathrm{f}(N, \mathrm{PWV})$ by use of Eq. (7) for different values of N ($N \leq N_\mathrm{max}$). Hence, the optimized error ϵ will result in minimizing ϵ_f whilst reducing N (see Fig. 2b).

$$\begin{aligned}\epsilon^2 &= \min[\epsilon_\mathrm{f}^2(N, \mathrm{PWV})] \\ &= \min[\sigma^2(N, \mathrm{PWV}) + \epsilon_\mathrm{s}^2(N)],\end{aligned} \tag{19}$$

where ϵ_f is the final error defined in Eq. (7), σ is the propagated uncertainty (Eq. 8) and ϵ_s is the sampling error (Eq. 18). The optimum number of samples N_0 will be defined as the argument of the minimum in Eq. (19).

$$N_0 = \arg\min[\epsilon_\mathrm{f}] \tag{20}$$

Finally, we can calculate the individual contribution of the uncertainty and the sampling error to the optimized error by means of

$$\begin{aligned}\sigma_0 &= \sigma(N_0, \mathrm{PWV}), \\ \epsilon_{s_0} &= \epsilon_s(N_0).\end{aligned} \tag{21}$$

5 Results

In this section we apply the method described above to the radiosounding dataset from ORM, GUI, LIN and NYA. In Table 2 we present a summary of the main statistical results for each location. The four sites show different behaviours in both the atmospheric PWV distribution and concentration. ORM and NYA show low contents of PWV, ORM being the driest site. Although the results cannot be taken as a climatic result, owing to the limitations in the sampling periods, they highlight the qualitative differences between the sites and help to discuss the results obtained in the error analyses. We also discuss the empirical estimation of the parameters needed in the models used by the method at each site. All the numerical results are listed in the Appendix B.

5.1 Exponential autocorrelation lags results

Figure 3 shows the results of τ_ρ estimated from the autocorrelation decay curves obtained from the radiosounding data at each location, as explained in Sect. 3.2. The empirical average curves show good agreement with the exponential fits (red and blue lines, respectively, in Fig. 3). The values of τ_ρ are also shown in the figure. The results are mainly related to the average PWV vertical distribution over each site. In the Canary Islands, this distribution is governed by the presence of the IL (see Sect. 1.2), which induces an abrupt decay in the WV that explains the lower values of τ_ρ and the maximum lag where the autocorrelation falls below 0.2 for GUI and

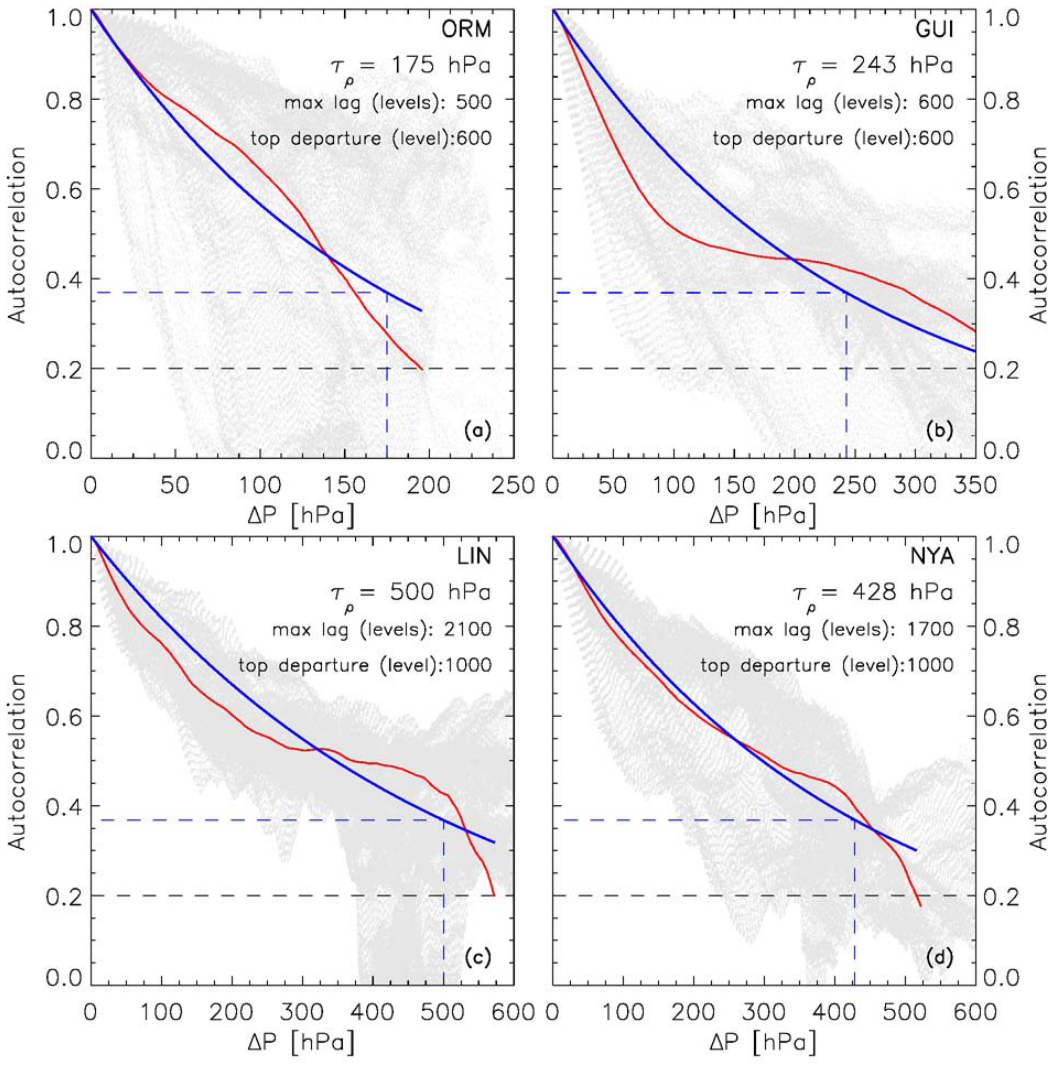

Figure 3. Results of the empirical autocorrelation exponential decay model applied of the four sites studied and exponential autocorrelation pressure lag (see Sect. 3.2). The background grey lines are the autocorrelations ρ_{ij} between a sub-sample of r_i from all the available radiosoundings and the following r_j, separated by the lag $\Delta P = p_i - p_j$. For each fixed lag, the departure levels i were sequentially shifted up to $\rho_{ij} = 0.2$, with a maximum level such as the level + lag approximately reach the troposphere height where the content of water vapour drops.

ORM. In particular, for the ORM this result is in agreement with the excellent conditions for IR astronomy (Hammersley, 1998) and with the low altitude reported for the tropopause by García-Lorenzo et al. (2004).

5.2 Sampling errors results

Figure 4 shows the best fits achieved to the residuals of the sub-sampling process applied at each location (see Sect. 3.3). The coefficients obtained are also shown in the figure. The first coefficient s_0 governs the rapid expansion of the sampling errors for sample sizes $\gtrsim N_0$. This coefficient is proportional to the average PWV (see Table 2); therefore, the more humid the atmosphere, the faster the sample error grows. The results are in concordance with the median PWV shown in Table 2, the driest sites being ORM and NYA, the ones with lower s_0. The coefficient s_1 governs the lower part of the curves, for sample sizes $\ll N_0$. It may be associated with uniformity in the vertical distribution of PWV. For an inhomogeneous vertical PWV distribution the sampling error is more sensitive to the shortage of measures when the number of levels is below the minimum N_0. The results show the lowest value for LIN and the largest for GUI, where the IL tend to break the PWV profile abruptly.

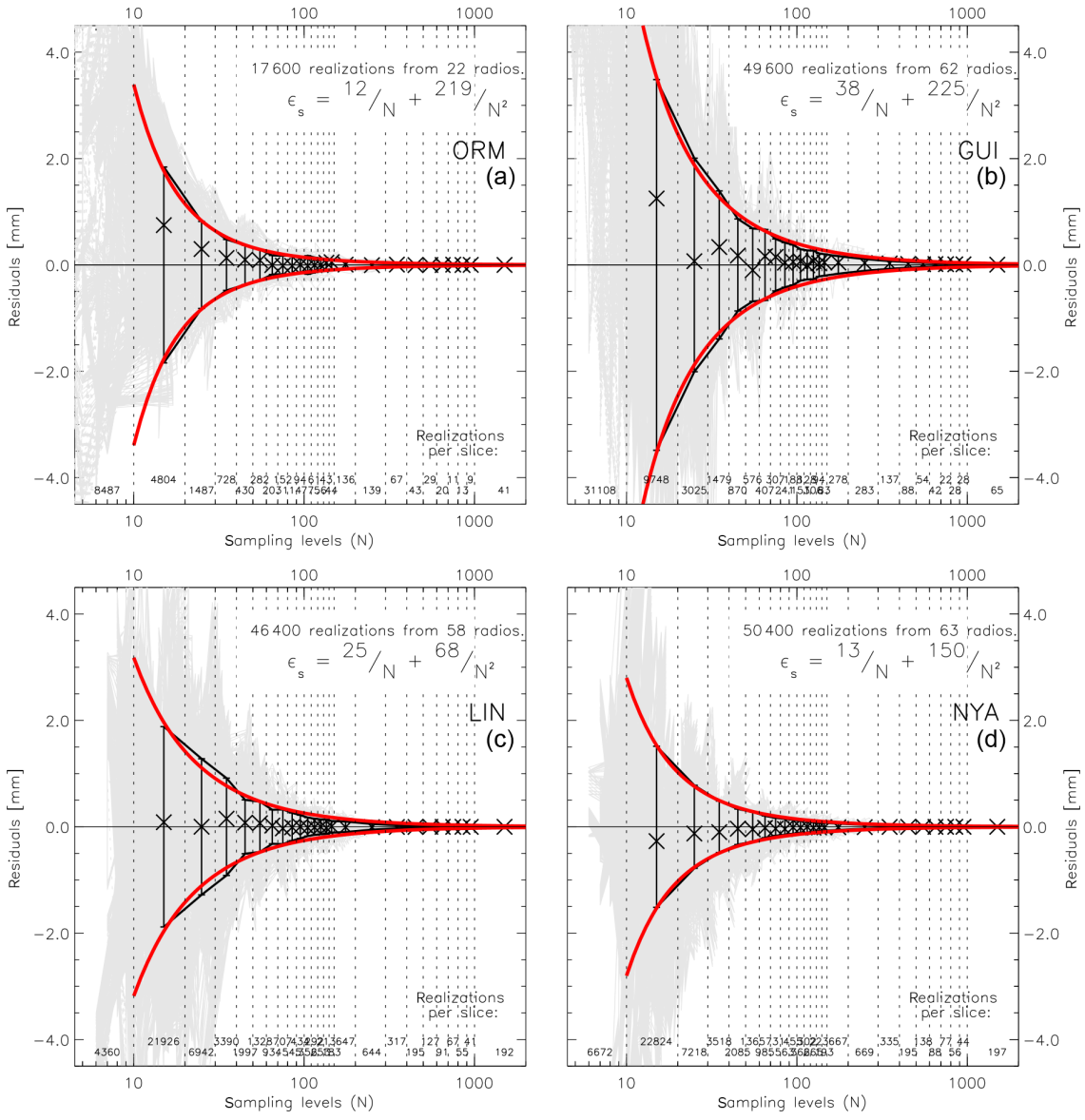

Figure 4. Results of the sample error model fit for the four sites studied (Eq. 18). The symbols and lines are the same than in Fig. 2a.

Table 2. PWV statistics (mm) for the four sites: percentiles (P_{xx}), median (med), minimum (min), maximum (max) and dispersion (s). The dispersion has been estimated robustly by means of $1.4826 \times$ MAD, where MAD is the median absolute deviation and 1.4826 is the scale factor between MAD and the standard deviation for perfect Gaussian distributions.

Site	n	Min	P_{10}	P_{25}	Med − s	Med	Med + s	P_{75}	P_{90}	Max
ORM	22	0.89	1.9	2.79	1.87	4.14	6.41	6.08	9.51	12.96
GUI	62	9.34	11.3	14.43	11.77	18.40	25.03	23.13	26.56	41.11
LIN	58	3.33	6.9	8.95	6.63	13.54	20.44	18.01	26.01	33.83
NYA	63	1.45	2.9	5.81	4.14	8.87	13.60	12.46	16.38	18.07

5.3 Optimized error results

We have applied the optimization described in Sect. 4 to all the available radiosondes and locations. For each profile, we have computed Eq. (7) recursively while sub-sampling the profile and carrying out the minimization in Eq. (19) with the local values of τ_ρ, s_0 and s_1 (see Figs. 3 and 4). Figure 5 shows six particular examples, focused on the Canarian

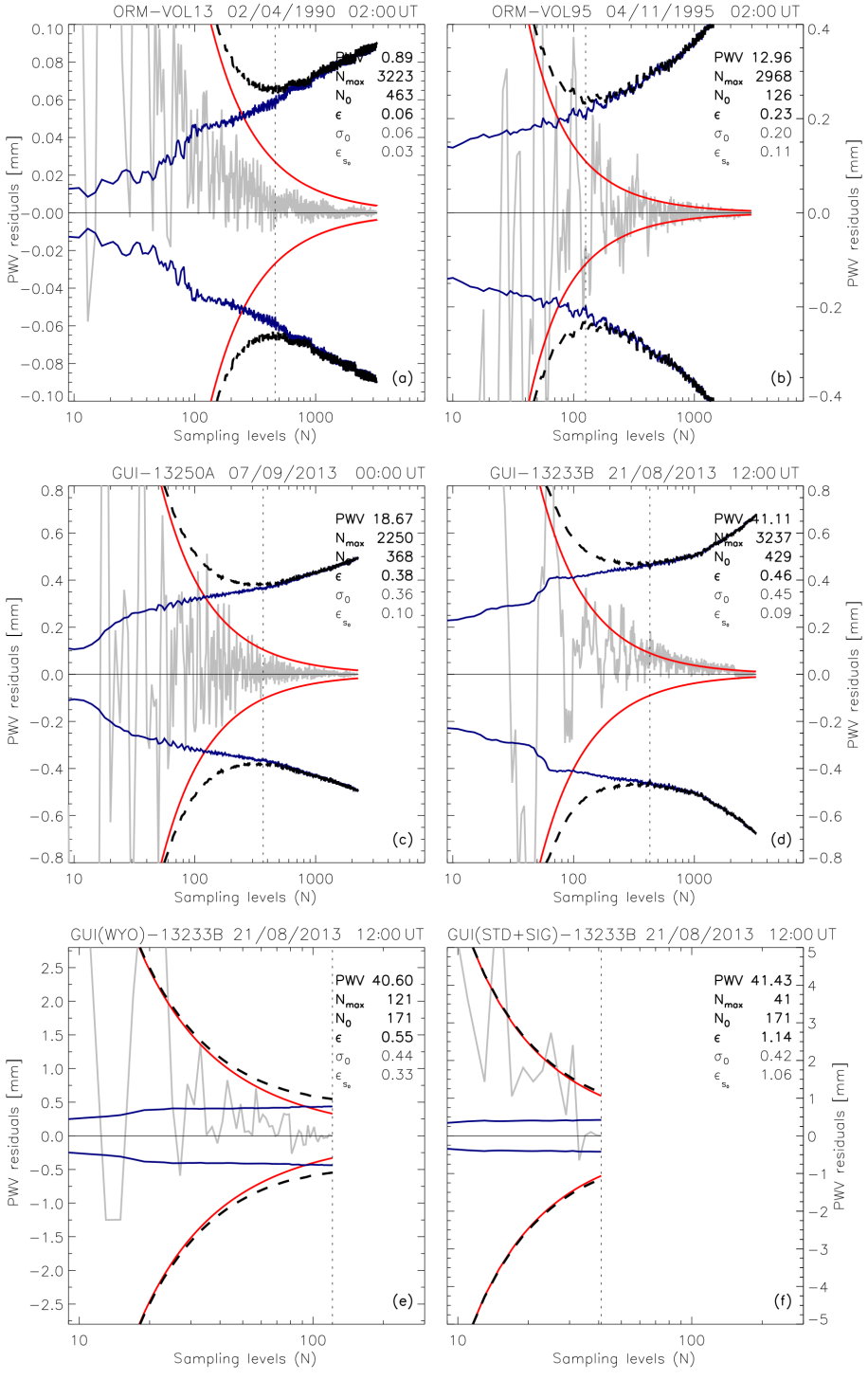

Figure 5. Six graphic examples with the application of the method of sub-sampling error optimization for ORM **(a)** and **(b)** and GUI **(c)** and **(d)**, with different PWV concentrations and $N_{\max} \gg N_0$. Panels **(e)** and **(f)** show the same profile as **(d)** but from data from the WYO repository (see Sect. 1.1), where $N_{\max} \approx N_0$ and with the SD + SIG levels ($N_{\max} < N_0$). The solid grey line shows the residual between the sub-sampled PWV estimation and the best value with all the levels available. The vertical dotted lines are the optimized number of samples for the minimum error. The PWV and errors in the legend are in millimetres.

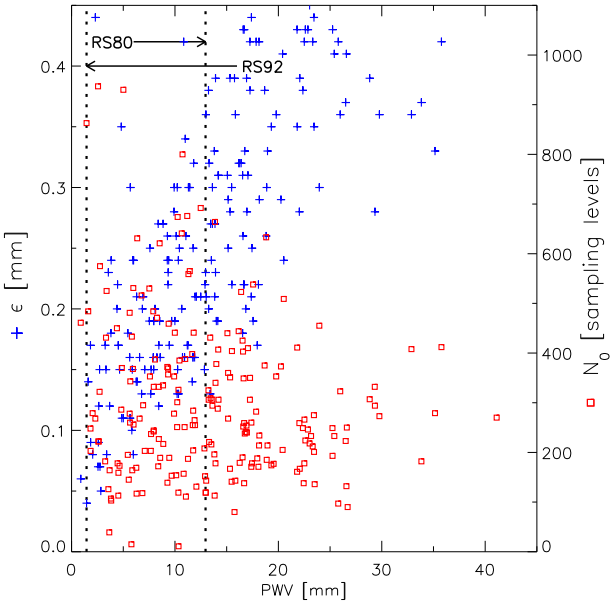

Figure 6. Optimized error ϵ (blue pluses and left axis) and optimum number of samples N_0 (red squares and right axis) for all the available radiosondes as a function of the PWV value. The ranges of values covered by the two models of radiosondes used (RS80 and RS90) is indicated with the grey arrows.

sites. The first two panels (Fig. 5a and b) show two results for the ORM, while the panels c and d are results for GUI. In both cases, we have selected two profiles with strong differences in the PWV content for each location. Additionally, in Fig. 5e and f, we show the results of the method applied to the same profile in Fig. 5d, but now with the re-sampled data of WYO ($N_{\max} \approx N_0$) and the SD + SIG levels ($N_{\max} < N_0$; see Sect. 1.1). In all cases, the residuals oscillate inside the range defined by the sampling error model (red line in Fig. 5), while converging. For $N_{\max} \gg N_0$, the error is dominated by σ, whereas for $N_{\max} \approx N_0$ the sample error ϵ_s becomes significant. We sub-sampled the data in the profiles WYO and SD + SIG by extracting $N, N-2, N-4, \ldots$ points, uniformly distributed for each iteration, to obtain a sufficient number of realizations close to $N_{\max}$.

Figure 6 shows all the results. The values of ϵ and N_0 are plotted together for all the available radiosondes as a function of PWV. The optimized error ϵ is roughly proportional to PWV, whereas N_0 is the reverse. The optimum sampling number N_0 is less than 400 for 77 % of the radiosoundings (see Fig. 6 and Appendix B for the numerical values). As we are using two different sonde models (RS80 and RS92), we have indicated the range of values covered for each. No differences or any bias as a function of the profile were observed.

We obtained errors less than $\sim$ 0.6 mm for all cases; this is significantly lower than the 1.3 mm error published by Liu et al. (2000), also taking into account the sampling effect in the error, but with no deeper analyses into the dependence on N. Specifically for the sampling component ϵ_{s_0}, we also obtained a lower average value of 0.11 mm with a maximum of 0.29 mm (except for some outliers found in the

Table 3. Relative error (ϵ_{rel}) statistics (%): percentiles 10th and 90th (P_{xx}), median (med), minimum (min), maximum (max) and dispersion (s). The dispersion has been estimated robustly by means of 1.4826 × MAD, where MAD is the median absolute deviation and 1.4826 is the scale factor between MAD and the standard deviation for perfect Gaussian distributions.

Min	P_{10}	Med − s	Med	Med + s	P_{90}	Max
0.9 %	1.3 %	1.3 %	2.0 %	2.7 %	4.6 %	67.2 %

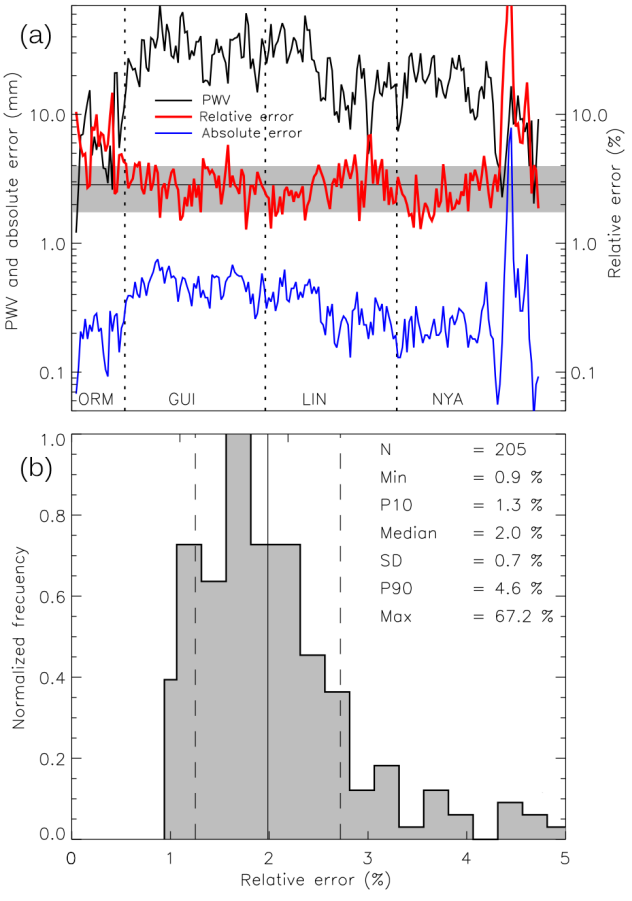

Figure 7. Relative error (ϵ_{rel}) statistics. Panel **(a)** shows all the PWV values (black), plotted together with their absolute (blue) and relative errors (red) in a logarithm scale. The thin horizontal line and shadow show the median relative error and dispersion. The dispersion has been estimated robustly by means of 1.4826 × MAD, where MAD is the median absolute deviation and 1.4826 is the scale factor between MAD and the standard deviation for perfect Gaussian distributions. Panel **(b)** shows the histogram of the distribution of relative errors. The vertical lines show the median value and dispersion range (dashed). The main statistics is in the legend.

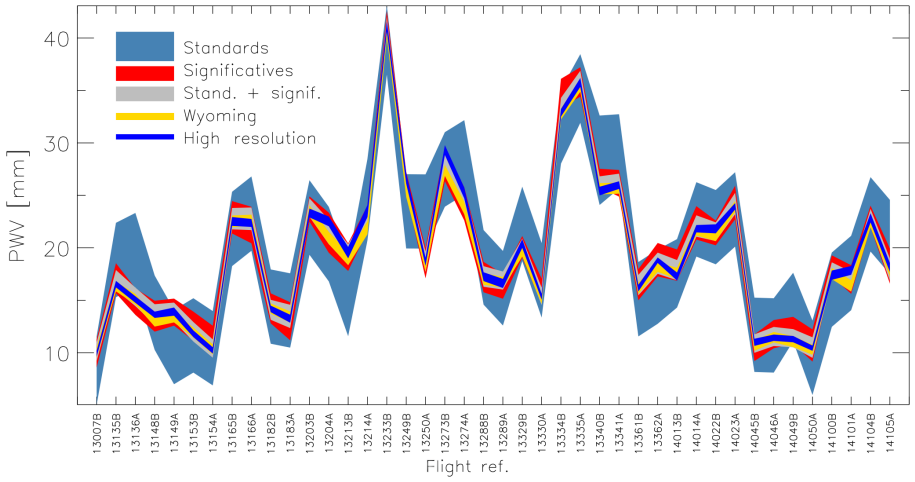

Figure 8. Comparison between the PWV series and errors (shadow) obtained from the GUI data with high-resolution radiosoundings (> 2500 levels) and different sub-extractions of the same profiles. The colour code, from the less to the most sampled series, is in the legend. The labels in the x axis are the references for each balloon flight (see Table B2).

NYA sample), in comparison to 0.50 and $\approx$ 1 mm, respectively, obtained by Liu et al. (2000) after analysing the residuals between the smoothed data (the standard output) and the much denser real-time records from 50 PWV radiosoundings in Hong Kong.

Figure 7 and Table 3 summarize the statistical results for the relative errors ($\epsilon_{\rm rel}$ hereafter) for the whole dataset of 205 radiosoundings. Relative errors behave in a slightly opposite way to the absolute optimized errors ϵ: the drier the atmosphere, the larger the $\epsilon_{\rm rel}$ (see Fig. 7a). The median relative error is $2.0 \pm 0.7\,\%$, and the 90th percentile $P_{90} = 4.6\,\%$. Around 10 outlier points have been obtained in the relative errors for NYA, mainly concentrated in the winter period (in the extreme case the relative error reaches 67.2 %). These values are not valid error estimates and define the limits of the model based on empirical data. Visual inspection of the mixing ratio profiles corresponding to those dates shows abrupt irruptions of extremely humid layers in the upper levels. This feature is related to the atmospheric circulation in the extreme conditions during the winter months at the Arctic latitude of NYA and goes far beyond the average conditions for which the parameters τ_ρ, s_0 and s_1 were estimated for that location. Therefore, for these points, the simplified pure exponential autocorrelation model fails and a new model, based on knowledge of the specific local atmospheric conditions, must to be implemented.

The complete list of $\epsilon_{\rm rel}$ is also included in Appendix B. These results reduce by more than a half the uncertainty of $\approx 5\,\%$ ($\approx 15\,\%$ for extremely dry conditions) published by Schneider et al. (2010) following the mixing ratio uncertainties obtained by Miloshevich et al. (2009) from the Vaisala RS92 RH sensors and highlight the importance of optimized sampling in the PWV determinations from radiosoundings.

5.4 Validation for poorly sampled radiosonde data ($N_{\rm max} < N_0$)

To validate the model, we have compared the errors obtained for the high-resolution radiosoundings of GUI with the same profiles with different re-samplings (WYO, SD + SIG, SIG and SD). The ~ 15 SD levels are the minima and mandatory levels reported by the radiosondes and may be considered the most pessimistic scenario ($N_{\rm max} \ll N_0$). In this case, the sampling component dominates ($\epsilon \approx \epsilon_{\rm s}$) and the error can be directly estimated from Eq. (18) with $N = N_{\rm max}$. For SIG and SD + SIG the situation is gradually more favourable, but still ($N_{\rm max} < N_0$). Finally, in the WYO data, the sampling approximates to N_0.

The results of the comparison[6] are shown in the Fig. 8. In the four cases, the error of the less sampled series includes the PWV and error estimates of the next series up to the high-resolution profiles. Therefore, the modelled errors statistically represent the differences between the calculated PWV and the best available estimate. The relative errors for the GUI-SD series range between ~ 5 and $\sim 30\,\%$. Therefore, Fig. 8 also evidences the ability of the standard levels to reproduce the tendencies in long-term PWV monitoring programmes.

6 Conclusions

We have considered a semiempirical approximation to the error propagation for PWV determinations from radiosonde profiles. To do this, we have considered two terms in the error estimation: the uncertainties in the measures σ and the

[6]The flight 13335A has been removed from the GUI-SD series because the first standard level is missed.

sampling error ϵ_s (the whole atmospheric column is assumed to be uniformly sampled). Moreover, the uncertainty contribution is separated into variance and covariance components. The variance has been estimated by means of analytical error propagation through all the levels sampled by the balloon, avoiding the correlation between adjacent bins. In contrast, the covariance and the sampling error have been empirically modelled at four locations – in the Canary Islands, Germany and the Svalbard Islands – with different datasets of radiosoundings ranging over 1 year. The covariance model is based on the exponential decay of the autocorrelation function, while the sampling error model is based on the number of samples of the composite trapezoidal formulas for numerical integration and their errors.

The uncertainty σ increases and ϵ_s decreases as the number of sampled levels grows. Therefore, we have optimized the error by gradually reducing the number of samples N. The optimization leads to the calculation of the minimum error (Eq. 19) and may be considered an appropriate estimator of the error in the PWV determination. The value of N in the minimum error is the optimum number of samples N_0 (Eq. 20).

The parameters estimated to fit the empirical models are governed by the average PWV content and its distribution. From the values obtained in the four sites studied, the ORM is the driest location with the fastest vertical decay of PWV.

The sub-sampling minimization was applied to all the radiosoundings in the datasets. The results show a coherent behaviour with no differences or bias as a function of the profile. The optimized error ϵ is roughly proportional to PWV, whereas N_0 is the reverse. The value of N_0 is less than 400 for 77 % of the profiles and the absolute errors are always < 0.6 mm, with the sampling component $\epsilon_{s_0} < 0.3$ mm.

Two different scenarios arise after the determination of N_0, whether the actual number of levels in the profile $N_{\max}$ is greater or equal than N_0 or not. For $N_{\max} \geq N_0$ it is always possible to reach N_0 by sub-sampling and therefore to obtain the minimum error. For $N_{\max} < N_0$ the sampling component dominates and the final error can be obtained directly from the model (Eq. 18).

The method was validated by the comparison of poorly sampled profiles and high-vertical-resolution data. The results showed that the high-resolution PWV values fall inside the interval defined by the low-resolution PWV values $\pm$ the estimated errors. The errors grew by up to > 30 % with poorly sampled profiles for dry atmospheres. The median relative error for high-resolution profiles is 2.0 ± 0.9 %, with 90th percentile $P_{90} = 4.6$ %. These results reduce by more than a half the uncertainties previously reported in the literature.

Therefore, not only the uncertainties define the error in PWV estimations from radiosoundings but also the autocorrelation between levels and the sampling. Here we have proposed that it is possible to optimize the number of sampled levels to minimize the error within the instrumental uncertainty. Whereas a radiosounding samples at least N_0 uniform vertical levels, depending on the WV content and distribution of the atmosphere, the error in the PWV estimate is likely to stay below ≈ 3 % (median + dispersion = 2.7 %) even for dry conditions.

7 Data availability

The radiosonde balloons were launched at the ORM by the IAC and the University of Nice under the direction of Jean Vernin (jean.vernin@unice.fr) and Casiana Muñoz-Tuñón (cmt@iac.es), with support from the Centre National de Recherches Météorologiques5 (Météo-France). Soundings at Güímar are launched and verified by the Spanish Agencia Estatal de Meteorología (AEMet; http://www.aemet.es). The sounding data at Lindenberg and Ny-Ålesund have been compiled and verified by the GCOS Reference Upper-Air Network (GRUAN; http://www.dwd.de/EN/research/international_programme/gruan/home.html). The low-resolution radiosounding data are available through the page of the Dept. of Atmospheric Science at the University of Wyoming (http://weather.uwyo.edu/upperair/sounding.html).

Appendix A: Variance of the trapezoidal rule integration for experimental data

Let y be an experimental variable measured at certain discrete points x_i. Let us assume that y and x are independent, as we are working with experimental data. Let $\sigma_{y,i}$ and $\sigma_{x,i}$ be the uncertainties associated with y_i and x_i. The trapezoidal rule of integration approximates as follows:

$$I = \int_a^b y\,\mathrm{d}x \approx \frac{1}{2}\sum_{i=0}^{N-1}(y_{i+1}+y_i)\cdot(x_{i+1}-x_i), \tag{A1}$$

The data are grouped into bins, such that the values in the right side of one bin are shared in the left side of the following bin. This binning effect adds a covariance term with a correlation of unity. To avoid this correlation we must eliminate the double summation of consecutive layers. We can write the Eq. (A1) in the following form:

$$\begin{aligned} I \approx \frac{1}{2}\Big[&y_0(x_1-x_0)+y_N(x_N-x_{N-1}) \\ &+\sum_{i=0}^{N-1} y_i(x_{i+1}-x_{i-1})\Big] \\ =\frac{1}{2}&\left(I_0+I_N+I_i\right). \end{aligned} \tag{A2}$$

Applying the chain rule leads to

$$\mathrm{var}_I = \sigma_I^2 = \frac{1}{4}\left(\sigma_{I,0}^2+\sigma_{I,N}^2+\sigma_{I,i}^2\right) = \sigma_{I_y}^2+\sigma_{I_x}^2, \tag{A3}$$

where

$$\sigma_{I,0}^2 = \sigma_{y,0}^2(x_1-x_0)^2 + f(\sigma_{x,0},\sigma_{x,1},y_0), \tag{A4}$$

$$\sigma_{I,N}^2 = \sigma_{y,N}^2(x_N-x_{N-1})^2 + f(\sigma_{x,N},\sigma_{x,N-1},y_N) \tag{A5}$$

$$\begin{aligned} \sigma_{I,i}^2 = &\sum_{i=0}^{N-1}\sigma_{y,i}^2(x_{i+1}-x_{i-1})^2 \\ &+\sum_{i=0}^{N-1} f(\sigma_{x,i+1},\sigma_{x,i-1},y_i). \end{aligned} \tag{A6}$$

Therefore,

$$\begin{aligned} \sigma_{I_y}^2 = \frac{1}{4}\Big[&\sigma_{y,0}^2(x_1-x_0)^2+\sigma_{y,N}^2(x_N-x_{N-1})^2 \\ &+\sum_{i=0}^{N-1}\sigma_{y,i}^2(x_{i+1}-x_{i-1})^2\Big]. \end{aligned} \tag{A7}$$

We can now write Eq. (A1) in the following form:

$$\begin{aligned} I \approx \frac{1}{2}\Big[&-x_0(y_1+y_0)+x_N(y_N+y_{N-1}) \\ &-\sum_{i=0}^{N-1} x_i(y_{i+1}-y_{i-1})\Big], \end{aligned} \tag{A8}$$

from which follows

$$\begin{aligned} \sigma_{I_x}^2 = \frac{1}{4}\Big[&\sigma_{x,0}^2(y_1+y_0)^2+\sigma_{x,N}^2(y_N+y_{N-1})^2 \\ &+\sum_{i=0}^{N-1}\sigma_{x,i}^2(y_{i+1}-y_{i-1})^2\Big]. \end{aligned} \tag{A9}$$

The final variance of I will then result after substituting Eqs. (A9) and (A7) into Eq. (A3).

Appendix B: Data compilation

The following tables show the PWV and associated errors for each sounding at ORM, GUI, LIN and NYA.

Table B1. PWV data and optimized error ϵ (see Eq. 19) for the radiosoundings at ORM. $N_{\max}$ is the actual number of sampled levels; H_t (m) and p_t (hPa) are the top height and pressure reached by the balloon. The parameters σ_0 and ϵ_{s_0} are the uncertainty and sampling components of the error (Eq. 21) and N_0 is the optimum number of levels (Eq. 20). The brackets in the last column are the relative errors ϵ_{rel}.

No.	Ref ORM	Date – time (Y/M/D – UTC)	$N_{\max}$	H_t (m)	p_t (hPa)	σ_0 (mm)	ϵ_{s_0} (mm)	N_0	PWV (mm)	ϵ (ϵ_{rel}) (mm; %)
1	VOL13	1990/04/02 – 02:00	3223	22685	37.4	0.06	0.03	461	0.89	0.06 (7.0)
2	VOL14	1990/04/02 – 05:00	3234	19757	60.1	0.06	0.06	203	1.84	0.09 (4.9)
3	VOL15	1990/04/03 – 00:00	3482	22455	38.7	0.14	0.08	159	4.53	0.17 (3.7)
4	VOL16	1990/04/03 – 03:00	3625	23284	33.7	0.13	0.08	173	4.64	0.15 (3.2)
5	VOL17	1990/04/05 – 04:00	2210	21429	45.6	0.18	0.12	117	6.29	0.21 (3.4)
6	VOL18	1990/07/13 – 22:00	2657	17797	83.7	0.14	0.05	242	7.94	0.15 (1.8)
7	VOL19	1990/07/17 – 02:00	7002	25537	24.2	0.17	0.09	153	9.68	0.19 (2.0)
8	VOL20	1990/07/18 – 00:00	4549	22648	37.9	0.16	0.07	182	3.25	0.17 (5.4)
9	VOL21	1990/07/20 – 02:00	4077	22749	37.2	0.21	0.07	178	4.45	0.22 (4.9)
10	VOL22	1990/07/21 – 00:00	2512	19646	61.3	0.20	0.11	126	3.56	0.23 (6.4)
11	VOL23	1990/07/21 – 03:00	3482	20683	51.6	0.12	0.12	113	4.52	0.17 (3.9)
12	VOL24	1990/07/21 – 22:00	4672	22542	38.5	0.13	0.13	107	3.81	0.18 (4.8)
13	VOL25	1990/07/22 – 03:00	3325	25818	23.1	0.11	0.06	222	2.63	0.12 (4.7)
14	VOL26	1990/07/22 – 22:00	4879	23126	35.2	0.07	0.06	222	2.59	0.09 (3.4)
15	VOL27	1990/07/23 – 01:00	4729	23793	31.7	0.07	0.05	279	2.04	0.08 (3.9)
16	VOL92	1995/11/01 – 11:00	3398	27987	15.7	0.19	0.14	103	3.83	0.24 (6.2)
17	VOL93	1995/11/03 – 00:00	3466	29257	12.9	0.16	0.05	248	1.83	0.17 (9.3)
18	VOL94	1995/11/03 – 22:00	2876	28593	14.4	0.20	0.09	152	12.91	0.22 (1.7)
19	VOL95	1995/11/04 – 02:00	2968	22755	35.5	0.20	0.12	119	12.96	0.23 (1.8)
20	VOL97	1995/11/08 – 23:00	3933	29481	12.1	0.09	0.08	164	3.68	0.12 (3.2)
21	VOL98	1995/11/09 – 01:00	3705	27971	15.6	0.16	0.07	195	5.44	0.18 (3.2)
22	VOL99	1995/11/09 – 04:00	4116	30828	10.2	0.16	0.12	118	6.85	0.20 (2.9)

Table B2. PWV data and optimized error ϵ (see Eq. 19) from the radiosoundings at GUI. See the caption of Table B1 for description.

No.	Ref GUI	Date – time (Y/M/D – UTC)	N_{max}	H_t (m)	p_t (hPa)	σ_0 (mm)	ϵ_{s_0} (mm)	N_0	PWV (mm)	ϵ (ϵ_{rel}) (mm; %)
1	13007B	2013/01/07 – 12:00	3056	31132	9.1	0.24	0.14	278	9.91	0.28 (2.8)
2	13135B	2013/05/15 – 12:00	2545	28793	14.1	0.29	0.09	425	16.54	0.31 (1.9)
3	13136A	2013/05/16 – 00:00	2637	29437	12.8	0.30	0.09	440	15.07	0.31 (2.1)
4	13148B	2013/05/28 – 12:00	2644	29995	11.9	0.27	0.13	294	13.62	0.30 (2.2)
5	13149A	2013/05/29 – 00:00	2720	28343	15.3	0.37	0.11	340	13.92	0.39 (2.8)
6	13153B	2013/06/02 – 12:00	2643	29319	13.1	0.31	0.09	441	11.81	0.32 (2.7)
7	13154A	2013/06/03 – 00:00	2706	29594	12.6	0.28	0.13	301	10.22	0.30 (3.0)
8	13165B	2013/06/14 – 12:00	2488	27297	18.0	0.35	0.22	178	22.51	0.42 (1.9)
9	13166A	2013/06/15 – 00:00	2978	30989	10.4	0.34	0.16	249	22.37	0.38 (1.7)
10	13182B	2013/07/01 – 12:00	2844	29560	12.9	0.30	0.09	407	14.18	0.31 (2.2)
11	13183A	2013/07/02 – 00:00	2925	29223	13.6	0.36	0.12	325	13.24	0.38 (2.9)
12	13203B	2013/07/22 – 12:00	2744	29786	12.5	0.38	0.18	212	23.32	0.42 (1.8)
13	13204A	2013/07/23 – 00:00	2918	30551	11.2	0.44	0.15	266	22.52	0.46 (2.0)
14	13213B	2013/08/01 – 12:00	2654	29736	12.6	0.50	0.22	177	19.54	0.54 (2.8)
15	13214A	2013/08/02 – 00:00	2436	25772	23.1	0.49	0.29	136	23.51	0.57 (2.4)
16	13233B	2013/08/21 – 12:00	3237	31950	9.0	0.44	0.14	270	41.11	0.47 (1.1)
17	13249B	2013/09/06 – 12:00	2244	27485	17.5	0.47	0.16	250	26.62	0.50 (1.9)
18	13250A	2013/09/07 – 00:00	2250	28271	15.5	0.37	0.10	375	18.67	0.38 (2.0)
19	13273B	2013/09/30 – 12:00	2653	29176	13.4	0.45	0.12	332	29.32	0.46 (1.6)
20	13274A	2013/10/01 – 00:00	2486	27200	18.1	0.49	0.16	249	25.23	0.51 (2.0)
21	13288B	2013/10/15 – 12:00	2746	29125	13.3	0.40	0.13	306	17.25	0.42 (2.4)
22	13289A	2013/10/16 – 00:00	2769	30299	11.2	0.40	0.15	252	16.60	0.43 (2.6)
23	13329B	2013/11/25 – 12:00	2662	27989	15.4	0.36	0.19	205	20.41	0.41 (2.0)
24	13330A	2013/11/26 – 00:00	2808	30105	11.1	0.26	0.11	351	15.33	0.28 (1.8)
25	13334B	2013/11/30 – 12:00	2448	28148	15.1	0.35	0.09	408	32.87	0.36 (1.1)
26	13335A	2013/12/01 – 00:00	2879	31302	9.4	0.41	0.09	412	35.77	0.42 (1.2)
27	13340B	2013/12/06 – 12:00	2091	23451	31.2	0.38	0.17	233	25.41	0.41 (1.6)
28	13341A	2013/12/07 – 00:00	2577	30067	11.3	0.34	0.12	323	25.98	0.36 (1.4)
29	13361B	2013/12/27 – 12:00	2660	30235	11.3	0.31	0.09	444	16.16	0.32 (2.0)
30	13362A	2013/12/28 – 00:00	2530	29248	13.0	0.25	0.06	633	18.82	0.26 (1.4)
31	14013B	2014/01/13 – 12:00	2798	31080	9.9	0.36	0.11	350	17.26	0.38 (2.2)
32	14014A	2014/01/14 – 00:00	2873	30890	10.2	0.34	0.09	411	21.82	0.35 (1.6)
33	14022B	2014/01/22 – 12:00	2722	26329	20.0	0.36	0.24	161	21.81	0.43 (2.0)
34	14023A	2014/01/23 – 00:00	2730	27670	16.2	0.29	0.08	455	23.96	0.30 (1.3)
35	14045B	2014/02/14 – 12:00	2710	29279	13.0	0.33	0.10	388	10.99	0.34 (3.1)
36	14046A	2014/02/15 – 00:00	2822	30141	11.4	0.29	0.07	565	11.43	0.30 (2.6)
37	14049B	2014/02/18 – 12:00	2792	31016	9.8	0.29	0.07	559	11.30	0.30 (2.6)
38	14050A	2014/02/19 – 00:00	2693	28572	14.3	0.23	0.10	385	10.43	0.25 (2.4)
39	14100B	2014/04/10 – 12:00	3109	29384	12.4	0.42	0.15	260	17.39	0.44 (2.5)
40	14101A	2014/04/11 – 00:00	2816	29287	12.7	0.39	0.14	282	17.85	0.42 (2.3)
41	14104B	2014/04/14 – 12:00	2942	29719	12.0	0.40	0.16	246	22.86	0.43 (1.9)
42	14105A	2014/04/15 – 00:00	2988	30894	10.1	0.38	0.18	214	18.13	0.42 (2.3)

Table B2. Continued.

No.	Ref GUI	Date – time (Y/M/D – UTC)	N_{max}	H_t (m)	p_t (hPa)	σ_0 (mm)	ϵ_{s_0} (mm)	N_0	PWV (mm)	ϵ (ϵ_{rel}) (mm; %)
43	13137A	2013/05/17 – 00:00	2610	29672	12.4	0.27	0.10	373	20.25	0.29 (1.4)
44	13150A	2013/05/30 – 00:00	2865	30415	11.2	0.30	0.09	410	17.06	0.31 (1.8)
45	13155A	2013/06/04 – 00:00	2332	25585	23.3	0.31	0.24	167	15.32	0.39 (2.6)
46	13167A	2013/06/16 – 00:00	2656	28438	15.3	0.33	0.25	157	10.84	0.42 (3.8)
47	13184A	2013/07/03 – 00:00	2907	31220	10.1	0.39	0.17	224	22.61	0.43 (1.9)
48	13205A	2013/07/24 – 00:00	2743	30442	11.4	0.43	0.29	138	22.45	0.52 (2.3)
49	13215A	2013/08/03 – 00:00	2556	25626	23.6	0.43	0.17	233	23.16	0.46 (2.0)
50	13251A	2013/09/08 – 00:00	2473	29406	13.1	0.41	0.14	275	23.44	0.44 (1.9)
51	13275A	2013/10/02 – 00:00	2891	31355	9.7	0.38	0.20	193	25.24	0.43 (1.7)
52	13290A	2013/10/17 – 00:00	2846	29637	12.3	0.40	0.15	259	16.69	0.43 (2.6)
53	13331A	2013/11/27 – 00:00	2540	27461	16.6	0.36	0.15	254	16.92	0.39 (2.3)
54	13336A	2013/12/02 – 00:00	2510	27390	17.0	0.29	0.14	279	35.15	0.33 (0.9)
55	13342A	2013/12/08 – 00:00	2452	26832	18.5	0.37	0.13	307	28.83	0.39 (1.4)
56	13363A	2013/12/29 – 00:00	2655	28921	13.7	0.27	0.06	664	13.87	0.27 (2.0)
57	14015A	2014/01/15 – 00:00	2611	30027	11.6	0.31	0.07	523	16.40	0.32 (1.9)
58	14024A	2014/01/24 – 00:00	2765	30428	10.6	0.21	0.06	692	12.49	0.21 (1.7)
59	14047A	2014/02/16 – 00:00	2494	28342	14.8	0.20	0.11	357	9.34	0.23 (2.5)
60	14051A	2014/02/20 – 00:00	2447	26572	19.5	0.28	0.13	306	14.21	0.31 (2.2)
61	14102A	2014/04/12 – 00:00	2609	29792	11.8	0.41	0.18	218	23.02	0.45 (1.9)
62	14106A	2014/04/16 – 00:00	2822	30473	10.8	0.35	0.11	353	19.79	0.36 (1.8)

Table B3. PWV data and optimized error ϵ (see Eq. 19) from the radiosoundings at LIN. See the caption of Table B1 for description.

No.	Ref LIN	Date – time (Y/M/D – UTC)	N_{max}	H_t (m)	p_t (hPa)	σ_0 (mm)	ϵ_{s_0} (mm)	N_0	PWV (mm)	ϵ (ϵ_{rel}) (mm; %)
1	13135B	2013/05/15 – 12:00	5349	31832	9.1	0.23	0.09	268	15.14	0.25 (1.6)
2	13136A	2013/05/16 – 00:00	5160	29464	13.0	0.27	0.14	185	18.87	0.30 (1.6)
3	13137A	2013/05/17 – 00:00	7343	35835	5.3	0.26	0.09	294	29.34	0.28 (0.9)
4	13148B	2013/05/28 – 12:00	6175	34617	6.5	0.32	0.11	238	16.75	0.33 (2.0)
5	13149A	2013/05/29 – 00:00	7120	36042	5.3	0.24	0.05	509	20.52	0.24 (1.2)
6	13150A	2013/05/30 – 00:00	6734	33123	8.0	0.26	0.10	259	22.03	0.28 (1.3)
7	13153B	2013/06/02 – 12:00	6938	34644	6.5	0.33	0.26	97	25.79	0.42 (1.6)
8	13154A	2013/06/03 – 00:00	5727	25603	24.2	0.35	0.09	273	29.77	0.36 (1.2)
9	13155A	2013/06/04 – 00:00	4288	19270	64.6	0.38	0.29	90	26.70	0.48 (1.8)
10	13165B	2013/06/14 – 12:00	6839	35303	6.1	0.28	0.07	360	15.14	0.29 (1.9)
11	13166A	2013/06/15 – 00:00	8384	37041	4.8	0.25	0.11	240	16.96	0.28 (1.6)
12	13167A	2013/06/16 – 00:00	8155	36319	5.3	0.31	0.15	174	19.32	0.35 (1.8)
13	13182B	2013/07/01 – 12:00	6811	32838	8.7	0.33	0.13	201	23.45	0.35 (1.5)
14	13184A	2013/07/03 – 06:00	6155	32287	9.4	0.36	0.15	167	22.07	0.39 (1.8)
15	13203B	2013/07/22 – 12:00	6537	33690	7.8	0.27	0.11	234	18.16	0.29 (1.6)
16	13204A	2013/07/23 – 00:00	7457	36860	5.0	0.31	0.12	214	18.95	0.33 (1.8)
17	13205A	2013/07/24 – 00:00	6875	36293	5.4	0.23	0.18	141	15.48	0.30 (1.9)
18	13213B	2013/08/01 – 12:00	7064	34940	6.5	0.34	0.14	182	33.83	0.37 (1.1)
19	13214A	2013/08/02 – 06:00	6236	32066	9.7	0.35	0.11	223	26.51	0.37 (1.4)
20	13215A	2013/08/03 – 06:00	6301	32477	9.1	0.36	0.19	132	26.58	0.41 (1.5)
21	13233B	2013/08/21 – 12:00	5184	29218	14.5	0.29	0.14	179	16.26	0.32 (2.0)
22	13249B	2013/09/06 – 12:00	5839	33715	7.2	0.31	0.18	143	15.84	0.36 (2.3)
23	13250A	2013/09/07 – 00:00	7284	34846	6.1	0.30	0.11	221	13.30	0.32 (2.4)
24	13251A	2013/09/08 – 00:00	7607	36811	4.6	0.28	0.21	119	12.99	0.36 (2.7)
25	13273B	2013/09/30 – 12:00	6191	32818	7.7	0.19	0.07	387	8.07	0.20 (2.5)
26	13274A	2013/10/01 – 00:00	7445	35144	5.5	0.18	0.04	621	8.52	0.19 (2.2)
27	13275A	2013/10/02 – 00:00	7064	34287	6.3	0.15	0.05	471	8.26	0.16 (1.9)
28	13288B	2013/10/15 – 18:00	5238	26684	18.5	0.26	0.06	403	16.58	0.26 (1.6)
29	13289A	2013/10/16 – 00:00	6974	36149	4.3	0.21	0.07	349	16.64	0.22 (1.3)
30	13290A	2013/10/17 – 00:00	5248	28313	14.0	0.26	0.08	309	13.45	0.27 (2.0)
31	13329B	2013/11/25 – 12:00	7562	36374	3.8	0.13	0.04	631	6.35	0.14 (2.1)
32	13330A	2013/11/26 – 00:00	7223	34190	5.5	0.12	0.05	516	6.77	0.13 (2.0)
33	13331A	2013/11/27 – 00:00	6722	35594	4.6	0.15	0.05	481	5.62	0.16 (2.8)
34	13334B	2013/11/30 – 12:00	7051	35870	4.1	0.20	0.04	641	10.66	0.20 (1.9)
35	13335A	2013/12/01 – 00:00	7010	35161	4.5	0.21	0.07	369	9.33	0.22 (2.4)
36	13336A	2013/12/02 – 00:00	7356	36557	3.6	0.19	0.09	295	6.92	0.21 (3.1)
37	13340B	2013/12/06 – 12:00	7420	36059	3.6	0.18	0.05	530	7.52	0.19 (2.5)
38	13341A	2013/12/07 – 00:00	6505	32573	6.3	0.10	0.03	930	5.01	0.11 (2.1)
39	13342A	2013/12/08 – 00:00	6423	33786	5.4	0.24	0.05	459	9.39	0.24 (2.6)
40	13361B	2013/12/27 – 12:00	6692	34137	5.3	0.24	0.07	353	7.58	0.25 (3.3)

Table B3. Continued.

No.	Ref LIN	Date – time (Y/M/D – UTC)	N_{max}	H_t (m)	p_t (hPa)	σ_0 (mm)	ϵ_{s_0} (mm)	N_0	PWV (mm)	ϵ (ϵ_{rel}) (mm; %)
41	13362A	2013/12/28 – 00:00	6847	33214	5.9	0.31	0.13	196	13.81	0.33 (2.4)
42	13363A	2013/12/29 – 00:00	6454	30862	8.6	0.19	0.05	538	17.56	0.19 (1.1)
43	14014A	2014/01/14 – 00:00	5669	33323	6.9	0.24	0.09	284	11.76	0.25 (2.2)
44	14015A	2014/01/15 – 00:00	6793	34574	5.6	0.18	0.07	378	14.00	0.19 (1.4)
45	14022B	2014/01/22 – 12:00	5637	32604	7.4	0.18	0.08	332	7.95	0.19 (2.4)
46	14023A	2014/01/23 – 00:00	5600	29472	11.8	0.14	0.06	431	3.33	0.15 (4.5)
47	14024A	2014/01/24 – 00:00	6737	35096	4.6	0.19	0.06	450	4.39	0.20 (4.5)
48	14045B	2014/02/14 – 12:00	6775	35616	5.3	0.15	0.05	484	7.90	0.16 (2.0)
49	14046A	2014/02/15 – 00:00	7060	38019	3.7	0.29	0.07	353	9.92	0.30 (3.1)
50	14047A	2014/02/16 – 00:00	7321	37788	3.8	0.25	0.08	306	13.62	0.27 (2.0)
51	14049B	2014/02/18 – 12:00	6311	33854	6.7	0.23	0.07	372	9.26	0.24 (2.6)
52	14050A	2014/02/19 – 00:00	6365	33836	6.6	0.26	0.08	335	8.85	0.27 (3.0)
53	14051A	2014/02/20 – 00:00	6078	31672	9.0	0.16	0.04	676	11.19	0.17 (1.5)
54	14101A	2014/04/11 – 00:00	6915	35621	5.1	0.20	0.17	154	10.12	0.26 (2.6)
55	14102A	2014/04/12 – 00:00	6854	35221	5.4	0.21	0.06	404	15.51	0.22 (1.4)
56	14104B	2014/04/14 – 12:00	5733	35001	5.6	0.18	0.06	441	9.99	0.19 (1.9)
57	14105A	2014/04/15 – 00:00	6731	34832	5.7	0.15	0.04	674	10.26	0.15 (1.5)
58	14106A	2014/04/16 – 00:00	7198	35327	5.3	0.16	0.03	800	10.73	0.16 (1.5)

Table B4. PWV data and optimized error ϵ (see Eq. 19) from the radiosoundings at NYA. See the caption of Table B1 for description.

No.	Ref NYA	Date – time (Y/M/D – UTC)	N_{max}	H_t (m)	p_t (hPa)	σ_0 (mm)	ϵ_{s_0} (mm)	N_0	PWV (mm)	ϵ (ϵ_{rel}) (mm; %)
1	13124A	2013/05/04 – 00:00	5914	30671	11.0	0.11	0.03	370	4.86	0.11 (2.3)
2	13136B	2013/05/16 – 12:00	5970	32028	9.5	0.10	0.05	260	5.66	0.11 (2.0)
3	13148B	2013/05/28 – 12:00	8489	33551	8.0	0.11	0.06	203	7.66	0.13 (1.7)
4	13153B	2013/06/02 – 12:00	7974	34785	6.8	0.19	0.09	143	13.02	0.21 (1.6)
5	13165B	2013/06/14 – 12:00	6624	30024	13.4	0.11	0.04	332	8.43	0.12 (1.4)
6	13182B	2013/07/01 – 12:00	6736	29671	14.3	0.20	0.05	241	16.85	0.20 (1.2)
7	13203B	2013/07/22 – 12:00	7141	34032	7.8	0.20	0.08	171	18.07	0.22 (1.2)
8	13205B	2013/07/24 – 12:00	5595	33221	8.7	0.13	0.03	431	13.41	0.13 (1.0)
9	13215B	2013/08/03 – 12:00	7983	35292	6.4	0.23	0.12	111	11.06	0.26 (2.3)
10	13233B	2013/08/21 – 12:00	5799	33178	8.2	0.19	0.04	306	13.26	0.20 (1.5)
11	13247A	2013/09/04 – 00:00	6555	34689	6.2	0.16	0.07	188	17.96	0.17 (0.9)
12	13248A	2013/09/05 – 00:00	7556	36242	4.9	0.13	0.03	398	11.67	0.14 (1.2)
13	13249A	2013/09/06 – 00:00	6502	34268	6.5	0.15	0.05	251	10.93	0.16 (1.5)
14	13249B	2013/09/06 – 12:00	5902	32373	8.7	0.15	0.06	204	11.76	0.16 (1.4)
15	13250A	2013/09/07 – 00:00	6019	32781	8.1	0.14	0.06	208	12.85	0.15 (1.2)
16	13251A	2013/09/08 – 00:00	6074	32896	7.9	0.17	0.07	190	16.54	0.18 (1.1)
17	13252A	2013/09/09 – 00:00	6978	30734	10.9	0.19	0.08	171	17.38	0.21 (1.2)
18	13253A	2013/09/10 – 00:00	5831	30156	11.9	0.15	0.07	189	8.57	0.16 (1.9)
19	13253B	2013/09/10 – 12:00	6616	33213	7.5	0.15	0.05	255	11.72	0.16 (1.3)
20	13254A	2013/09/11 – 00:00	6333	34318	6.3	0.15	0.07	187	11.26	0.17 (1.5)
21	13255A	2013/09/12 – 00:00	6100	32492	8.2	0.25	0.09	139	9.27	0.26 (2.8)
22	13257A	2013/09/14 – 00:00	6572	34439	6.1	0.16	0.06	227	8.44	0.17 (2.0)
23	13258A	2013/09/15 – 00:00	6186	33099	7.4	0.13	0.04	326	10.34	0.13 (1.3)
24	13260A	2013/09/17 – 00:00	5348	36169	4.5	0.21	0.05	255	11.94	0.21 (1.8)
25	13260B	2013/09/17 – 12:00	6735	33459	7.0	0.20	0.09	138	16.69	0.22 (1.3)
26	13261A	2013/09/18 – 00:00	6614	33915	6.5	0.18	0.04	288	14.14	0.19 (1.3)
27	13262A	2013/09/19 – 00:00	6054	33707	6.7	0.18	0.12	113	13.84	0.21 (1.5)
28	13263A	2013/09/20 – 00:00	6391	34536	5.9	0.24	0.07	178	17.45	0.25 (1.4)
29	13263B	2013/09/20 – 12:00	7966	35783	4.9	0.23	0.06	216	13.52	0.24 (1.8)
30	13264A	2013/09/21 – 00:00	6405	34478	5.9	0.22	0.07	178	13.92	0.23 (1.7)
31	13265A	2013/09/22 – 00:00	7055	33585	6.7	0.18	0.05	244	7.95	0.19 (2.3)
32	13266A	2013/09/23 – 00:00	7003	33483	6.7	0.12	0.05	251	10.21	0.13 (1.3)
33	13268A	2013/09/25 – 00:00	7218	34099	5.9	0.15	0.05	268	6.58	0.16 (2.4)
34	13268B	2013/09/25 – 12:00	4659	24903	24.9	0.13	0.06	203	7.08	0.15 (2.1)
35	13269A	2013/09/26 – 00:00	6530	33493	6.4	0.12	0.08	164	5.87	0.15 (2.5)
36	13269B	2013/09/26 – 12:00	6586	33807	6.1	0.11	0.08	169	6.26	0.14 (2.2)
37	13270A	2013/09/27 – 00:00	7151	33408	6.4	0.15	0.07	189	9.45	0.17 (1.8)
38	13271A	2013/09/28 – 00:00	6639	33269	6.5	0.21	0.11	119	10.33	0.24 (2.3)
39	13272A	2013/09/29 – 00:00	7019	33973	5.8	0.26	0.07	172	8.38	0.27 (3.2)
40	13273A	2013/09/30 – 00:00	6791	32790	6.9	0.35	0.17	80	15.76	0.39 (2.5)
41	13273B	2013/09/30 – 12:00	6550	32858	6.9	0.18	0.10	131	12.07	0.21 (1.7)
42	13274A	2013/10/01 – 00:00	6355	33166	6.5	0.15	0.05	265	11.90	0.16 (1.3)
43	13275A	2013/10/02 – 00:00	6846	32563	7.1	0.14	0.05	237	7.69	0.15 (1.9)
44	13288B	2013/10/15 – 12:00	5771	31255	8.0	0.07	0.02	525	3.39	0.08 (2.3)

Table B4. Continued.

No.	Ref NYA	Date – time (Y/M/D – UTC)	N_{max}	H_t (m)	p_t (hPa)	σ_0 (mm)	ϵ_{s_0} (mm)	N_0	PWV (mm)	ϵ (ϵ_{rel}) (mm; %)
45	13290B	2013/10/17 – 12:00	6211	32503	6.4	0.05	0.01	1243	2.83	0.05 (1.6)
46	13329B	2013/11/25 – 12:00	4685	26677	14.6	0.07	0.01	937	2.56	0.07 (2.9)
47	13334B	2013/11/30 – 12:00	6292	30330	7.5	0.14	0.03	484	1.61	0.14 (8.7)
48	13341B	2013/12/07 – 12:00	5613	28845	9.2	0.44	0.05	268	2.30	0.44 (19.0)
49	13362B	2013/12/28 – 12:00	4329	23972	20.8	1.04	0.41	39	3.65	1.12 (30.6)
50	14013B	2014/01/13 – 12:00	6554	31082	6.3	3.60	1.46	15	5.79	3.89 (67.2)
51	14022B	2014/01/22 – 12:00	5130	27781	10.6	4.61	2.32	11	10.35	5.17 (49.9)
52	14034A	2014/02/03 – 00:00	6057	30568	7.4	0.56	0.09	145	5.53	0.57 (10.3)
53	14037A	2014/02/06 – 00:00	5137	29493	9.5	0.29	0.04	343	5.68	0.30 (5.2)
54	14041A	2014/02/10 – 00:00	5858	31060	7.1	0.49	0.06	217	8.87	0.49 (5.5)
55	14047B	2014/02/16 – 12:00	5142	27569	11.9	0.24	0.03	368	5.93	0.24 (4.1)
56	14050B	2014/02/19 – 12:00	5615	30130	8.3	0.23	0.05	256	6.00	0.24 (3.9)
57	14051B	2014/02/20 – 12:00	5432	28783	10.2	0.35	0.04	286	4.81	0.35 (7.2)
58	14053A	2014/02/22 – 00:00	5838	29669	8.4	0.62	0.05	278	5.62	0.62 (11.0)
59	14075A	2014/03/16 – 00:00	6110	30967	7.8	0.15	0.04	322	2.71	0.15 (5.7)
60	14100B	2014/04/10 – 12:00	5619	29207	13.2	0.10	0.03	433	5.83	0.10 (1.7)
61	14102B	2014/04/12 – 12:00	6904	33962	6.5	0.04	0.01	863	1.45	0.04 (2.8)
62	14104B	2014/04/14 – 12:00	6320	30732	10.6	0.07	0.02	575	2.75	0.07 (2.6)
63	14106B	2014/04/16 – 12:00	5833	33512	7.2	0.08	0.03	531	5.97	0.08 (1.4)

Acknowledgements. This work has been funded by the Instituto de Astrofísica de Canarias (IAC). Special thanks are due to the AEMet members Sergio Rodríguez, Ricardo Sanz, Ernesto Barrera and José María Rodríguez for their valuable suggestions, their diligence in the data transfer and extracting the significant levels from GUI. Special thanks are also given to Miguel Cerviño (IAC) for their valuable discussions and suggestions and to Terry Mahoney (IAC) for the English language correction. We finally would like to acknowledge the very constructive comments of the two anonymous referees that contributed to the improvement of the paper.

Edited by: S. Buehler
Reviewed by: T. Nilsson and one anonymous referee

References

Ahrens, C.: Meteorology Today: An Introduction to Weather, Climate, and the Environment, Brooks/Cole, 624 pp., 2003.

Barreto, A., Cuevas, E., Damiri, B., Guirado, C., Berkoff, T., Berjón, A. J., Hernández, Y., Almansa, F., and Gil, M.: A new method for nocturnal aerosol measurements with a lunar photometer prototype, Atmos. Meas. Tech., 6, 585–598, doi:10.5194/amt-6-585-2013, 2013.

Bevis, M., Businger, S., Herring, T. A., Rocken, C., Anthes, R. A., and Ware, R. H.: GPS Meteorology: Remote Sensing of Atmospheric Water Vapor Using the Global Positioning System, J. Geophys. Res.-Atmos., 97, 15787–15801 , doi:10.1029/92JD01517, 1992.

Bevis, M., Businger, S., Chiswell, S., Herring, T. A., Anthes, R. A., Rocken, C., and Ware, R. H.: GPS Meteorology: Mapping Zenith Wet Delays onto Precipitable Water, J. Appl. Meteorol., 33, 379–386, doi:10.1175/1520-0450(1994)033<0379:GMMZWD>2.0.CO;2, 1994.

Bird, R. E. and Hulstrom, R. L.: Precipitable Water Measurements with Sun Photometers, J. Appl. Meteorol., 21, 1196–1201, doi:10.1175/1520-0450(1982)021<1196:PWMWSP>2.0.CO;2, 1982.

Carilli, C. L. and Holdaway, M. A.: Tropospheric phase calibration in millimeter interferometry, Radio Sci., 34, 817–840, doi:10.1029/1999RS900048, 1999.

Carrillo, J., Guerra, J. C., Cuevas, E., and Barrancos, J.: Characterization of the Marine Boundary Layer and the Trade-Wind Inversion over the Sub-tropical North Atlantic, Bound.-Lay. Meteorol., 158, 311–330, doi:10.1007/s10546-015-0081-1, 2016.

Curry, J. and Webster, P.: Thermodynamics of atmospheres and oceans, Volume 65, International Geophysics series, Academic Press, San Diego, 1999.

Deeter, M. N.: A new satellite retrieval method for precipitable water vapor over land and ocean, Geophys. Res. Lett., 34, L02815, doi:10.1029/2006GL028019, 2007.

Dirksen, R. J., Sommer, M., Immler, F. J., Hurst, D. F., Kivi, R., and Vömel, H.: Reference quality upper-air measurements: GRUAN data processing for the Vaisala RS92 radiosonde, Atmos. Meas. Tech., 7, 4463–4490, doi:10.5194/amt-7-4463-2014, 2014.

Dorta, P.: Las inversiones térmicas en Canarias, Investigaciones Geográficas, 15, 109–124, 1996.

Dragosavac, M.: BUFR User's Guide, Technical note, European Centre for Medium-Range Weather Forecasts, 2007.

Elliott, W. P. and Gaffen, D. J.: Chapman Conference Probes Water Vapor in the Climate System, Eos T. Am. Geophys. Un., 76, p. 67, doi:10.1029/EO076i007p00067, 1995.

Firsov, K., Chesnokova, T., Bobrov, E., and Klitochenko, I.: Total water vapor content retrieval from sun photometer data, Atmos. Ocean. Opt., 26, 281–284, doi:10.1134/S1024856013040040, 2013.

Flatau, P., Walko, R., and Cotton, W.: Polynomial fits to saturation vapor pressure, J. Appl. Meteor., 31, 1507–1513, 1992.

Fowle, F. E.: The Spectroscopic Determination of Aqueous Vapor, Astrophys. J., 35, p. 149, doi:10.1086/141923, 1912.

Gao, B.-C. and Kaufman, Y. J.: Water vapor retrievals using Moderate Resolution Imaging Spectroradiometer (MODIS) near-infrared channels, J. Geophys. Res.-Atmos., 108, 4389, doi:10.1029/2002JD003023, 2003.

García-Lorenzo, B., Eff-Darwich, A., Castro-Almazán, J., Pinilla-Alonso, N., Muñoz-Tuñón, C., and Rodríguez-Espinosa, J. M.: Infrared astronomical characteristics of the Roque de los Muchachos Observatory: precipitable water vapour statistics, MNRAS, 405, 2683–2696, 2010.

García-Lorenzo, B. M., Fuensalida, J. J., and Eff-Darwich, A. M.: The role of the tropopause layer altitude on the infrared quality of astronomical sites, in: Optics in Atmospheric Propagation and Adaptive Systems VII, edited by: Gonglewski, J. D. and Stein, K., 384–391, doi:10.1117/12.565659, 2004.

Grody, N. C., Gruber, A., and Shen, W. C.: Atmospheric Water Content over the Tropical Pacific Derived from the Nimbus-6 Scanning Microwave Spectrometer, J. Appl. Meteorol., 19, 986–996, doi:10.1175/1520-0450(1980)019<0986:AWCOTT>2.0.CO;2, 1980.

Guiraud, F. O., Howard, J., and Gogg, D. C.: A dual-channel microwave radiometer for measurement of precipitable water vapor and liquid, IEEE T. Geosci. Elect., 17, 129–136, 1979.

Hammersley, P. L.: Infrared quality of the Canarian skies, New Astron. Rev., 42, 533–536, doi:10.1016/S1387-6473(98)00067-0, 1998.

Immler, F. J., Dykema, J., Gardiner, T., Whiteman, D. N., Thorne, P. W., and Vömel, H.: Reference Quality Upper-Air Measurements: guidance for developing GRUAN data products, Atmos. Meas. Tech., 3, 1217–1231, doi:10.5194/amt-3-1217-2010, 2010.

Kurylo, M. J.: Network for the detection of stratospheric change (NDSC), in: Remote Sensing of Atmospheric Chemistry, edited by: McElroy, J. L. and McNeal, R. J., Society of Photo-Optical Instrumentation Engineers (SPIE) Conference Series, 1491, 168–174, 1991.

Liu, Y., Chen, Y., and Baki Iz, H.: Precision of precipitable water vapor from radiosonde data for GPS solutions, Geomatica, 54, 171–175, 2000.

Menzel, W. P., Holt, F. C., Schmit, T. J., Aune, R. M., Schreiner, A. J., Wade, G. S., and Gray, D. G.: Application of GOES-8/9 Soundings to Weather Forecasting and Nowcasting, B. Am. Meteorol. Soc., 79, 2059–2078, doi:10.1175/1520-0477(1998)079<2059:AOGSTW>2.0.CO;2, 1998.

Miloshevich, L. M., Vömel, H., Paukkunen, A., Heymsfield, A. J., and Oltmans, S. J.: Characterization and Correction of Relative Humidity Measurements from Vaisala RS80-A Radiosondes at Cold Temperatures, J. Atmos. Ocean. Tech., 18, 135–156,

doi:10.1175/1520-0426(2001)018<0135:CACORH>2.0.CO;2, 2001.

Miloshevich, L. M., VöMel, H., Whiteman, D. N., Lesht, B. M., Schmidlin, F. J., and Russo, F.: Absolute accuracy of water vapor measurements from six operational radiosonde types launched during AWEX-G and implications for AIRS validation, J. Geophys. Res.-Atmos., 111, D09S10, doi:10.1029/2005JD006083, 2006.

Miloshevich, L. M., VöMel, H., Whiteman, D. N., and Leblanc, T.: Accuracy assessment and correction of Vaisala RS92 radiosonde water vapor measurements, J. Geophys. Res.-Atmos., 114, D11305, doi:10.1029/2008JD011565, 2009.

Otárola, A., Travouillon, T., Schöck, M., Els, S., Riddle, R., and Skidmore, W.: Thirty meter telescope site testing X: precipitable water vapor, PASP, 122, 470–484, 2010.

Pérez-Jordán, G., Castro-Almazán, J. A., Muñoz-Tuñón, C., Codina, B., and Vernin, J.: Forecasting the precipitable water vapour content: validation for astronomical observatories using radiosoundings, Mon. Not. R. Astron. Soc., 452, 1992–2003, doi:10.1093/mnras/stv1394, 2015.

Plana-Fattori, A., Legrand, M., Tanré, D., Devaux, C., Vermeulen, A., and Dubuisson, P.: Estimating the Atmospheric Water Vapor Content from Sun Photometer Measurements, J. Appl. Meteorol., 37, 790–804, doi:10.1175/1520-0450(1998)037<0790:ETAWVC>2.0.CO;2, 1998.

Romero-Campos, P. M., Marrero-de-la Santa-Cruz, C. L., Alonso-Pérez, S., Cuevas-Agulló, E., Afonso-Gómez, S., and Ortiz-de Galisteo-Marín, J. P.: Una Climatología del Agua Precipitable en la Región Subtropical sobre la Isla de Tenerife basada en Datos de Radiosondeos, Nota Técnica Nota Técnica AEMet No. 6, AEMet, available at: http://www.aemet.es/es/conocermas/publicaciones/detalles/NT6Aemet, 2011.

Schneider, M., Hase, F., and Blumenstock, T.: Water vapour profiles by ground-based FTIR spectroscopy: study for an optimised retrieval and its validation, Atmos. Chem. Phys., 6, 811–830, doi:10.5194/acp-6-811-2006, 2006.

Schneider, M., Romero, P. M., Hase, F., Blumenstock, T., Cuevas, E., and Ramos, R.: Continuous quality assessment of atmospheric water vapour measurement techniques: FTIR, Cimel, MFRSR, GPS, and Vaisala RS92, Atmos. Meas. Tech., 3, 323–338, doi:10.5194/amt-3-323-2010, 2010.

Selby, M. J. and Mampaso, A.: Infrared Observations in the Canary Islands, Astrophys. Lett. Comm., 28, 171–193, 1991.

Smith, G., Naylor, D., and Feldman, P.: Measurements of Atmospheric Water Vapor Above Mauna Kea Using an Infrared Radiometer, Int. J. Infrared Milli., 22, 661–678, doi:10.1023/A:1010689508585, 2001.

Vernin, J. and Muñoz-Tuñón, C.: Optical seeing at La Palma Observatory, I General guidelines and preliminary results at the Nordic Optical Telescope, Astron. Astrophys., 257, 811–816, 1992.

Vernin, J. and Muñoz-Tuñón, C.: Optical seeing at La Palma Observatory, II Intensive site testing campaign at the Nordic Optical Telescope, Astron. Astrophys., 284, 311–318, 1994.

Vernin, J., Muñoz-Tuñón, C., Sarazin, M., Vazquez Ramió, H., Varela, A. M., Trinquet, H., Delgado, J. M., Jiménez Fuensalida, J., Reyes, M., Benhida, A., Benkhaldoun, Z., García Lambas, D., Hach, Y., Lazrek, M., Lombardi, G., Navarrete, J., Recabarren, P., Renzi, V., Sabil, M., and Vrech, R.: European Extremely Large Telescope Site Characterization I: Overview, Publ. Astron. Soc. Pac., 123, 1334–1346, doi:10.1086/662995, 2011.

Volz, F. E.: Comments on "Precipitable Water Measurements with sun Photometers", J. Appl. Meteorol., 22, 1967–1968, doi:10.1175/1520-0450(1983)022<1967:COWMWS>2.0.CO;2, 1983.

Vömel, H., Selkirk, H., Miloshevich, L., Valverde-Canossa, J., Valdés, J., Kyrö, E., Kivi, R., Stolz, W., Peng, G., and Diaz, J. A.: Radiation Dry Bias of the Vaisala RS92 Humidity Sensor, J. Atmos. Ocean. Tech., 24, 953–963, doi:10.1175/JTECH2019.1, 2007.

Wong, M., Jin, X., Liu, Z., Nichol, J., Ye, S., Jiang, P., and Chan, P.: Geostationary Satellite Observation of Precipitable Water Vapor Using an Empirical Orthogonal Function (EOF) based Reconstruction Technique over Eastern China, Remote Sens., 7, 5879–5900, doi:10.3390/rs70505879, 2015.